MALT-45: A 7 mm survey of the southern Galaxy - I. Techniques and spectral line data

Christopher H. Jordan,[1,2]⋆ Andrew J. Walsh,[3] Vicki Lowe,[2,4] Maxim A. Voronkov,[2]
Simon P. Ellingsen,[1] Shari L. Breen,[2] Cormac R. Purcell,[5] Peter J. Barnes,[7]
Michael G. Burton,[4] Maria R. Cunningham,[4] Tracey Hill,[8] James M. Jackson,[9]
Steven N. Longmore,[6] Nicolas Peretto[10] and James S. Urquhart[11,2]

[1]*School of Physical Sciences, Private Bag 37, University of Tasmania, Hobart, Tasmania 7001, Australia*
[2]*CSIRO Astronomy and Space Science, PO Box 76, Epping, NSW 1710, Australia*
[3]*International Centre for Radio Astronomy Research, Curtin University, GPO Box U1987, Perth, WA 6845, Australia*
[4]*School of Physics, University of New South Wales, Sydney, NSW 2052, Australia*
[5]*School of Physics, University of Sydney, Sydney, NSW 2006, Australia*
[6]*Astrophysics Research Institute, Liverpool John Moores University, IC2, Liverpool Science Park, Liverpool L3 5RF, UK*
[7]*Astronomy Department, University of Florida, Gainesville, FL 32611, USA*
[8]*Joint ALMA Observatory, Alonso de Cordova 3107, Vitacura, Santiago, Chile*
[9]*Astronomy Department, Boston University, 725 Commonwealth Avenue, Boston, MA 02215, USA*
[10]*School of Physics & Astronomy, Cardiff University, Queens Buildings, The Parade, Cardiff CF24 3AA, UK*
[11]*Max-Planck-Institut für Radioastronomie, Auf dem Hügel 69, Bonn, Germany*

ABSTRACT

We present the first results from the MALT-45 (Millimetre Astronomer's Legacy Team - 45 GHz) Galactic Plane survey. We have observed 5 square-degrees ($l = 330 - 335$, $b = \pm 0.5$) for spectral lines in the 7 mm band (42–44 and 48–49 GHz), including CS (1–0), class I CH_3OH masers in the 7(0,7)–6(1,6) A^+ transition and SiO (1–0) $v = 0, 1, 2, 3$. MALT-45 is the first unbiased, large-scale, sensitive spectral line survey in this frequency range. In this paper, we present data from the survey as well as a few intriguing results; rigorous analyses of these science cases are reserved for future publications. Across the survey region, we detected 77 class I CH_3OH masers, of which 58 are new detections, along with many sites of thermal and maser SiO emission and thermal CS. We found that 35 class I CH_3OH masers were associated with the published locations of class II CH_3OH, H_2O and OH masers but 42 have no known masers within 60 arcsec. We compared the MALT-45 CS with NH_3 (1,1) to reveal regions of CS depletion and high opacity, as well as evolved star-forming regions with a high ratio of CS to NH_3. All SiO masers are new detections, and appear to be associated with evolved stars from the *Spitzer* Galactic Legacy Infrared Mid-Plane Survey Extraordinaire (GLIMPSE). Generally, within SiO regions of multiple vibrational modes, the intensity decreases as $v = 1, 2, 3$, but there are a few exceptions where $v = 2$ is stronger than $v = 1$.

Key words: masers – surveys – stars: formation – ISM: molecules – radio lines: ISM – Galaxy: structure

1 INTRODUCTION

High-mass stars are critical elements of Galactic structure, due to their evolution in molecular clouds, the turbulent energy they inject into the interstellar medium and the met-

als dispersed in their death. These stars are categorised by having mass $> 8M_\odot$ and eventually explode as type II supernovae, transforming the local interstellar medium.

The mechanism of high-mass star formation (HMSF) remains an important unsolved problem in astrophysics. Understanding HMSF is difficult for a number of reasons: the rarity of HMSF regions, high dust extinction within molec-

⋆ E-mail: christopher.jordan@utas.edu.au

ular clouds, rapid evolution, and large distances from our Solar System (Zinnecker & Yorke 2007) all combine to hinder our understanding. HMSF is known to begin within Giant Molecular Clouds (GMCs) and eventually end with star clusters or associations (Lada & Lada 2003). To understand the various stages of HMSF, an inventory of regions must be compiled in a range of known tracers.

To date, there have been many surveys conducted to help understand HMSF. These have been useful in identifying HMSF regions and their characteristic spectral lines, but tend to emphasise subsections of the HMSF timeline. Examples of these surveys include methanol masers (e.g. Walsh et al. 1998; Cyganowski et al. 2009; Green et al. 2009), infrared dark clouds (IRDCs; e.g. Peretto & Fuller 2009) and radio continuum sources (e.g. Purcell et al. 2013). Methanol masers act as reliable signposts of an early evolutionary stage of HMSF (Ellingsen 2006), but do not occur at every evolutionary stage; IRDCs are only seen when they are close to us, projected against a bright infrared background and are not always associated with HMSF (Kauffmann & Pillai 2010); radio continuum sources are powered by main sequence high-mass stars, and are seen only when their free-free emission has penetrated through the dense surroundings.

Large area surveys of molecular gas are ideal for identifying HMSF regions across a broad range of evolutionary phases. In particular, the critical density of a gas tracer can act as a probe for Galactic structure and star formation. Critical density (n_c) is a measure of the density required to produce detectable emission (Evans 1999). Previous surveys for star formation in external galaxies, typically for low-density gas tracers ($n_c < 10^3\,\mathrm{cm}^{-3}$), suffer from poor resolution (on the order of kpc) and sensitivity. Untargeted Galactic plane surveys avoid these issues, while simultaneously offering the ability to detect new, less obvious regions of star formation within our Galaxy. Other untargeted surveys have been productive in identifying extended emission, such as in CO (Dame, Hartmann & Thaddeus 2001; Jackson et al. 2006; Burton et al. 2013), OH (Dawson et al. 2014) and H I (McClure-Griffiths et al. 2005). However, HMSF occurs in regions of dense molecular gas, and so mapping high-density tracers serves well to identify target regions. CO (1–0) has a relatively low effective critical density ($n_c = {\sim}10^2\,\mathrm{cm}^{-3}$) compared to other tracers, such as NH$_3$ (1,1) (${\sim}10^3\,\mathrm{cm}^{-3}$; Evans 1999) and HC$_3$N (4–3) (${\sim}10^4\,\mathrm{cm}^{-3}$; Fuller & Myers 1993), which have been mapped by the H$_2$O Galactic Plane survey (HOPS; Walsh et al. 2011). HOPS has been successful in identifying previously unknown sites of star formation, as well as probing the structure of the Milky Way's spiral arms.

Another, even higher density gas tracer useful for detecting HMSF and mapping the structure of our Galaxy is CS. The ground state transition $J = (1-0)$ for CS lies within the 7 mm waveband, and has an effective critical density $n_c = 4.6 \times 10^4\,\mathrm{cm}^{-3}$ at 10 K (Evans 1999). Previous large scale observations towards specific regions, such as RCW 106 (Rodgers, Campbell & Whiteoak 1960) for CS and other high-critical-density molecules have been productive in HMSF research (Lo et al. 2009). Untargeted observations of CS over bright infrared regions such as RCW 106 and regions without infrared emission reveal the full population of star-forming candidates to a small sensitivity limit.

The 7 mm waveband also contains the 44 GHz 7(0,7)– 6(1,6) A$^+$ class I methanol maser line, which is the brightest of the class I species. Previous observations of the class I maser have almost always been targeted (e.g. Slysh et al. 1994; Voronkov et al. 2014), which limits and biases our understanding of this astrophysical phenomenon. The 7 mm waveband includes other spectral lines detailed in Table 1. To help develop our understanding of HMSF using the diagnostics in the 7 mm waveband, we have devised the MALT-45 untargeted Galactic plane survey.

1.1 Spectral lines

CS has a slightly higher effective critical density compared to NH$_3$ ($n_c = 4.6 \times 10^4\,\mathrm{cm}^{-3}$ vs. ${\sim}10^3\,\mathrm{cm}^{-3}$), but suffers from freeze-out on to dust grains in the coldest and most dense regions (Bergin et al. 2001). NH$_3$ appears to be resilient to freeze-out in these regions (Tafalla et al. 2002), therefore by comparing the dense gas tracers from MALT-45 and HOPS, we are able to identify these cold, dense regions in our Galaxy by analysing the CS/NH$_3$ ratio and NH$_3$ temperature. MALT-45 simultaneously surveys C^{34}S (1–0), which is a less abundant isotopologue of CS (assumed CS/C^{34}S ratio of 24.4; Chin et al. 1996). A comparison between CS and C^{34}S allows us to measure optical depth at these locations. C^{34}S data are not formally presented in this paper, but a preliminary data reduction has been performed for an optical depth investigation in Section 4.1.

There are two varieties of CH$_3$OH maser: class I and II. The class II variety is well known and studied; it is radiatively excited by young stellar objects with sufficient mass to be considered HMSF. Thus, it is vitally important as it occurs only in regions of HMSF, but only at a specific evolutionary state (Walsh et al. 1998; Minier et al. 2003; Green et al. 2012; Breen et al. 2013). In contrast, class I masers are poorly understood. Research has shown that the class I maser is collisionally excited, and associated with shocked gas (Voronkov et al. 2010a,b, 2014), but not necessarily only from outflows, as seen in Pihlström et al. (2014). It is known to occur in both low-mass (Kalenskii et al. 2010) and high-mass regions of star formation (Gan et al. 2013). Most known class I masers have been discovered in targeted searches towards other sources, such as 6.7 GHz class II masers (Ellingsen 2005), HMSF regions with and without UCH II regions (Kurtz, Hofner & Alvarez 2004) and extended green objects (EGOs; Cyganowski et al. 2008; Chen et al. 2011). Because class I masers have been found towards a range of sources and evolutionary states, their conditions for excitation remain uncertain. By conducting a sensitive and untargeted survey, MALT-45 reveals the full population of class I masers to a small sensitivity limit (5σ sensitivity of 4.5 Jy). This eliminates biases towards known tracers inherent in targeted observations, and helps understand their conditions of excitation.

SiO masers are commonly associated with oxygen rich Asymptotic Giant Branch (AGB) or Red Supergiant (RSG) stars, occurring in the extended atmosphere within a few stellar radii (Elitzur 1992; Messineo et al. 2002). These masers are useful in determining radial velocities to such stars to within a few km s^{-1} (Messineo et al. 2002). Messineo et al. (2002) conducted a survey for SiO masers at 86 GHz towards evolved stars, and demonstrated their use in probing

Galactic kinematics through the maser velocities. Additionally, SiO masers have been detected towards star-forming regions, but despite an extensive search towards a wide range of HMSF regions, only three are known (Orion Source I, W51 and Sgr B2; Zapata et al. 2009). SiO maser emission in Orion provides the best evidence of a high-mass accretion disc (Matthews et al. 2007). MALT-45 has the potential to reveal many new sources of SiO (1–0) maser emission, both towards evolved stars and star-forming regions.

Along with the maser emission, MALT-45 also includes SiO (1–0) $v = 0$, which is thermal line emission. Thermal SiO is commonly found in star-forming regions, produced when silicate-bearing grains are destroyed. Thus, it is a good tracer of shocked gas and outflows (Martin-Pintado, Bachiller & Fuente 1992).

In this paper, we focus on detailing the survey from $330° \leqslant l \leqslant 335°$, $b = \pm 0.5°$ and present results of the global properties of CS (1–0), class I CH_3OH masers and SiO (1–0) thermal and maser emission. This paper is one of a series; another paper will be dedicated to maser follow-up observations, and another for clump analysis with CS data. In this paper, we focus on comparing: CS emission to NH_3 and class I CH_3OH masers; class I CH_3OH masers to class II CH_3OH, H_2O and OH masers, thermal SiO and infrared emission, and 95 GHz class I CH_3OH masers; and SiO masers to infrared emission. We emphasise that the science cases presented in this paper are used primarily to highlight a few intriguing results and discuss some qualitatively plausible explanations. Full analyses for these cases will appear in future publications.

2 SURVEY DESIGN

MALT-45 is an untargeted Galactic plane survey for spectral lines which are commonly bright in star-forming regions at 45 GHz (7 mm waveband). We have so far observed 5 square-degrees within the region bounded by $330° \leqslant l \leqslant 335°$, $b = \pm 0.5°$. MALT-45 observations were conducted on the Australia Telescope Compact Array (ATCA), which provides $2 \times$ 2048 MHz broadband continuum windows for observing. Section 1.1 discusses the primary lines surveyed, and their rest frequencies dictate the positions of the broadband windows for MALT-45. Within the frequency ranges of the broadband windows, we survey for 12 spectral lines; see Table 1.

2.1 Australia Telescope Compact Array characterisation

The ATCA is an interferometer composed of six 22 m antennas, CA01 through CA06. In recent years, the ATCA correlator has been upgraded to the Compact Array Broadband Backend (CABB; Wilson et al. 2011), which now provides auto-correlation spectra. In addition to this upgrade, the ATCA obtained on-the-fly (OTF) mosaicing capabilities. We are particularly interested in the auto-correlations, as combining the six antennas in this way is similar to observing six times longer with an individual 22 m antenna such as Mopra. By using the ATCA auto-correlations for 7 mm surveying, we obtain an excellent metric on sensitivity versus survey speed. See Jordan et al. (2013) for pilot observations with MALT-45.
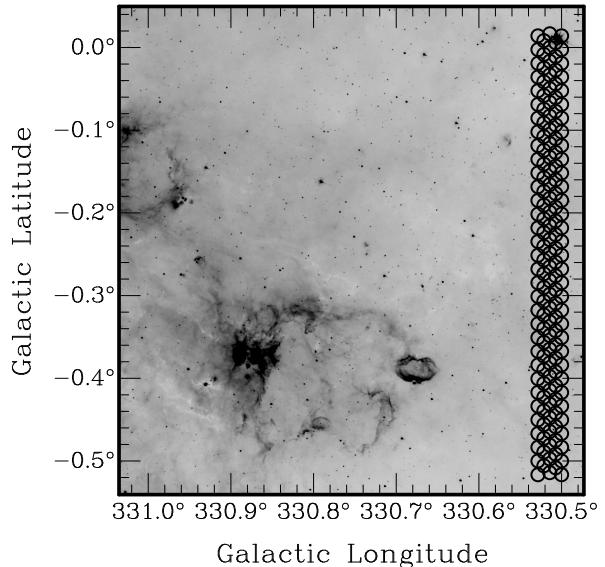

Figure 1. GLIMPSE $8.0 \, \mu m$ emission overlaid with part of a MALT-45 mosaic. Each circle represents the primary beam of the ATCA at 49.2 GHz, and is a pointing of the mosaic. Every quarter-square-degree region mapped by MALT-45 is built up of pointing "rows" seen here. These five rows represent the start of the Galactic latitude scans for the G330.5−0.5 region. A similar mosaic is made for each region in Galactic longitude. When both Galactic latitude and longitude mosaics are combined, a fully Nyquist sampled map is obtained. Rows are classified as either "long" or "short"; in this figure, the three long rows have two short rows interleaved.

For the results presented here, only data from antennas CA01 through CA05 are presented. CA06 has a higher surface root-mean-square (RMS) and poorer sensitivity in the 7 mm wavelength range. In future observations, it may be possible to include CA06 data by weighting its contribution accordingly, but it is ignored at present.

2.1.1 CABB zoom modes

The recent upgrades to the CABB correlator provide the option of observing with "zoom modes", which act as high-resolution spectral windows. MALT-45 makes use of the 64M-32k configuration. In addition to the two 2048 MHz broadband continuum windows, up to 16×64 MHz "zoom windows" can be allocated in each 2048 MHz range. Each zoom window has 2048 spectral channels, yielding a fine resolution of 32 kHz. At 45 GHz, this is approximately $0.2 \, km \, s^{-1}$ per channel. Each spectral line listed in Table 1 was observed with a 64M-32k zoom window (with the exception of the thermal CH_3OH 1_0–0_0 A^+ and E lines, which are separated by 4 MHz and were simultaneously observed within one zoom), using a total of 11 zooms. Each zoom window is ideally placed upon the spectral line centre frequency, although the exact placement depends on the way the correlator distributes the zooms. Every zoom provides approximately $400 \, km \, s^{-1}$ of velocity coverage, and is detailed in Table 1.

Table 1. Bright spectral lines mapped by MALT-45 between 42.2 and 49.2 GHz. The first column lists the spectral line. The second column lists the rest frequency of the line. The third column lists the uncertainty of the rest frequency. The fourth column classifies the line as either a maser or thermal line. The fifth column gives the ATCA pointing beam size at this frequency. The sixth column indicates whether this line is discussed in this paper ("Y") or not ("N"). Columns seven and eight detail the LSR velocity range covered by the CABB zoom band for this spectral line. The ninth column lists the median RMS noise level per spectral channel, with errors representing the standard deviation. The RMS noise is given to two significant figures. Radio recombination line (RRL) frequencies are taken from Lilley & Palmer (1968). All other rest frequencies are taken from the Cologne Database for Molecular Spectroscopy (CDMS; Müller et al. 2005). The velocity resolution ranges from $0.225 \, \text{km s}^{-1}$ (lowest rest frequency) to $0.195 \, \text{km s}^{-1}$ (highest rest frequency) per channel.

Spectral Line	Frequency (GHz)	Uncertainty (kHz)	Maser or thermal?	Beam Size (arcsec)	Detailed in this paper?	Velocity Range Min	Max (km s^{-1})	Median RMS Noise Level
SiO (1–0) $v = 3$	42.51934	1	Maser	66	Y	-287	167	0.85 ± 0.07 Jy
SiO (1–0) $v = 2$	42.82048	1	Maser	66	Y	-194	257	0.82 ± 0.06 Jy
H53 α (RRL)	42.95197		Thermal	65	N			
SiO (1–0) $v = 1$	43.12203	2	Maser	65	Y	-321	127	0.83 ± 0.06 Jy
SiO (1–0) $v = 0$	43.42376	2	Thermal	65	Y	-224	221	27 ± 1.7 mK
CH_3OH 7(0,7)–6(1,6) A^+	44.06941	10	Maser (Class I)	64	Y	-183	256	0.90 ± 0.09 Jy
H51 α (RRL)	48.15360		Thermal	58	N			
$C^{34}S$ (1–0)	48.20694	2	Thermal	58	N			
CH_3OH 1_0–0_0 A^+	48.37246	0.7	Thermal	58	N			
CH_3OH 1_0–0_0 E	48.37689	10	Thermal	58	N			
OCS (4–3)	48.65160	1	Thermal	58	N			
CS (1–0)	48.99095	2	Thermal	57	Y	-157	237	34 ± 6.8 mK

2.2 MALT-45 observations

All observations were conducted with the same surveying technique. Scans were observed in quarter-square-degree regions in Galactic coordinates, in both latitude and longitude directions. For both latitude and longitude scans, the mosaics are represented by "long" and "short" interleaved pointings. See Figure 1 for an illustrative example. Within a mosaic row, consecutive pointing centres are separated by 1.045 beams, and centres of each mosaic row are separated by 0.45 beams. Each beam (pointing) is observed for 6 seconds in OTF mode observing. The frequency used to calculate the size of the primary beam is 49.2 GHz (the highest observed frequency), thus the beam used was 57.13 arcsec, and separation parameters are 59.7 and 25.7 arcsec, respectively. When combined, the scans provide a fully Nyquist sampled spatial map.

The MALT-45 results presented here were observed over eight months on the ATCA. The first set of observations were conducted on 2012 September 21-23, 28 and 30, and October 1-13. The second set of observations were conducted from 2013 April 10-19. All observations were conducted in the H214 array configuration. The region $330° \leqslant l \leqslant 333°$, $b = \pm 0.5°$, and part of $333.0° \leqslant l \leqslant 333.5°$, $0° \leqslant b \leqslant 0.5°$ were surveyed in the first observing run. The remainder ($333° \leqslant l \leqslant 335°$, $b = \pm 0.5°$) was completed during the second observing run. Weather conditions across all observations were generally good, with typical path noises below $300 \, \mu\text{m}$. Path noise is a measure of the weather quality, based on the phase delay between successive measurements of a geosynchronous satellite. Values above $500 \, \mu\text{m}$ are generally considered poor, but conditions only affect interferometric data.

Each quarter square-degree region required approximately 14 hours observation time, including the typical setup and calibration. Pointing corrections were determined using PMN J1646−5044 and applied approximately every

70 minutes. The reference position G334.0−1.0 was observed every 45 minutes for calibration of the auto-correlation data. In addition, to allow interferometric calibration, bandpass calibration was derived from PKS B1253−055, phase calibration from PMN J1646−5044 and flux density from PKS 1934−63.

2.3 Data reduction

Data reduction was undertaken in a similar manner to that of the MALT-45 pilot survey (Jordan et al. 2013). Auto-correlations are extracted from the raw data using MIRIAD, before being converted into a single dish format. At this stage, the single dish data for each ATCA antenna is treated individually, using standard data reduction tools on a single dish such as Mopra. Each antenna has a baseline removal procedure applied using LiveData, followed by more robust baselining using the ATNF Spectral line Analysis Package (ASAP). ASAP averages each of the antenna auto-correlations together before performing further baseline smoothing. ASAP then provides both XX and YY polarisation products, which are used by Gridzilla to create data cubes.

Flux density calibration was achieved with antenna efficiencies and T_B-to-Jy conversion factors taken from Urquhart et al. (2010). Using these values assumes that the 7 mm antenna and receiver response from Mopra is similar to the ATCA. Once the data cubes were gridded, the factors were applied to provide appropriate flux density scaling.

The average RMS noise levels were calculated for each data cube. The median values and their errors are listed in Table 1. Values are calculated by using the MIRIAD task IMSTAT, which determines RMS values for each channel in a cube. Error values represent the standard deviation of all RMS values. RMS noise maps may be seen in Appendix A, Figures 1 through 6. Appendices are available online.
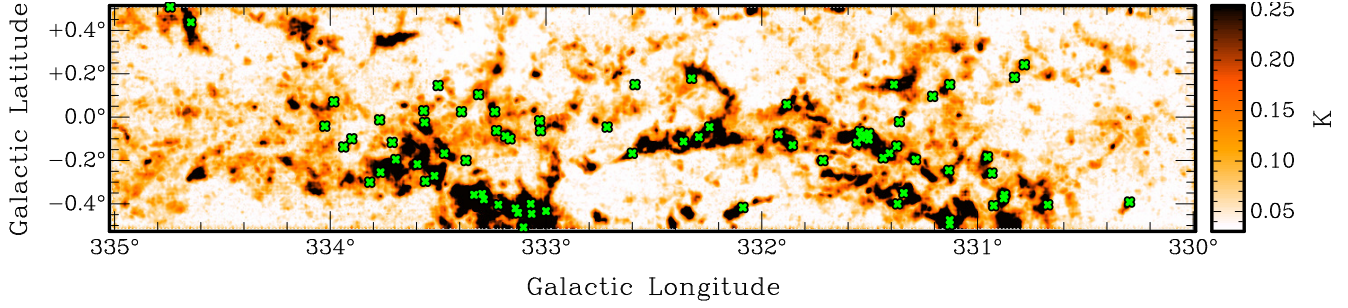
Figure 2: Auto-correlated CS (1–0) peak-intensity map overlaid with positions of detected class I CH$_3$OH masers (green cross symbols). A main-beam temperature of 0.1 K represents a 5σ peak of emission; note that the RMS of this image is less than that stated in Table 1 (20 mK vs. 34mK), because this image has been produced by binning channels into groups of 10.
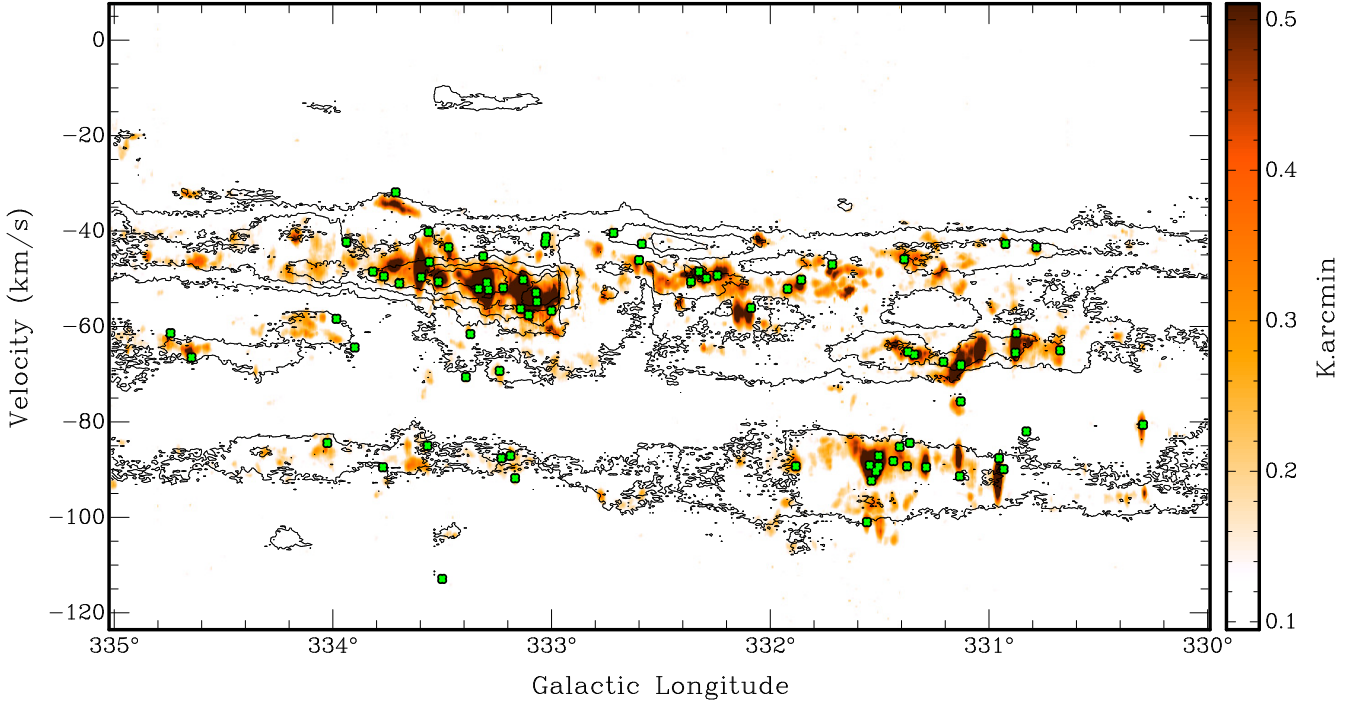
Figure 3: CS (1–0) from MALT-45 overlaid with CO contours from Barnes et al. (ApJ submitted). Contour levels are 90, 180, ...450 K arcmin in units of main-beam temperature, integrated over Galactic latitude. There is excellent agreement in regions of concentrated CO with CS emission. Green cross symbols represent MALT-45 class I CH$_3$OH masers, which generally occur in bright regions of CS; only 4 of the 77 masers (5 per cent) have a CS peak intensity less than 0.11 K ($\sim$3σ) at their peak position.
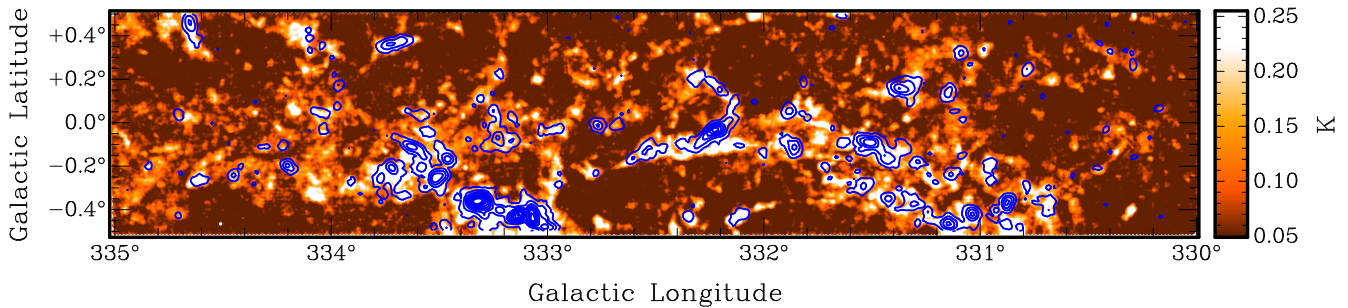
Figure 4: Auto-correlated CS (1–0) peak-intensity map overlaid with HOPS NH$_3$ (1,1) peak-signal-to-noise contours. Contour levels are 8, 18, ...88 per cent of 11.13 K in units of main-beam temperature. The white circle seen at G334.5−0.45 is the size of the beam.

3 RESULTS

For this paper, auto-correlated data cubes were produced for CS (1–0), class I CH$_3$OH masers, each of the SiO (1–0) $v = 1, 2, 3$ maser lines and SiO (1–0) $v = 0$ thermal emission. Emission was detected in each data cube. The absolute scale of intensity calibration is not well established, and can be affected by systematic effects such as the bandpass subtraction. However, comparing the peak flux densities of MALT-45 class I methanol masers with Voronkov et al. (2014), we ascribe 20 per cent as the uncertainty of the intensities in MALT-45 data.

The positions of class I methanol masers from MALT-45 and Voronkov et al. (2014) were compared to derive a survey astrometric error. The median RMS offset was determined by deriving the offset for each maser site in Voronkov et al. (2014) and the MALT-45 position. This median is 15 arcsec, and so we ascribe a 15 arcsec astrometric error to MALT-45.

3.1 CS (1–0) at 48.990 GHz

The most abundant isotopologue of CS (^{12}C^{32}S) was detected in extended emission across the entire survey region, as shown in Figures 2, 3 and 4. Also shown in Figure 4 is NH$_3$ (1,1) emission, as detected in HOPS (Purcell et al. 2012). Bright CS emission is largely coincident with HOPS NH$_3$ (1,1) emission, but despite having a higher critical density, the CS appears to be more extended than the NH$_3$; this is discussed further in Section 4.1. A longitude-velocity-latitude plot reveals a few velocity components to the CS data, which trace the spiral arms of the Galaxy over the survey region; see Figure 3.

C^{34}S (1–0) at 48.20694 GHz is also detected across the survey region, but is not detailed in this paper due to an incomplete data reduction. However, a preliminary reduction has been conducted for analysis in Section 4.1. C^{34}S data will be presented in future publications.

3.2 Class I CH$_3$OH 7(0,7)–6(1,6) A$^+$ masers at 44.069 GHz

Within the survey region, 77 class I CH$_3$OH masers were detected. Class I CH$_3$OH maser catalogues from Slysh et al. (1994); Val'tts et al. (2000); Ellingsen (2005) and Chen et al. (2011) were used to determine previously known masers. All 19 previously known masers were detected by MALT-45. Note that these articles report findings of 95 GHz class I CH$_3$OH masers, rather than 44 GHz masers (except Slysh et al. 1994); if a 44 GHz maser has not been reported in a position where a 95 GHz maser has been detected, we still deem this class I maser as a previously known detection. Therefore, 58 of the 77 detections are previously unknown (hereinafter new masers). A histogram of these populations can be seen in Figure 5, revealing the number of new masers for various peak flux densities. Images showing the locations of class I CH$_3$OH masers with respect to thermal molecular gas are shown in Figures 2, 3 and 6. The properties of each class I maser spectrum is classified in Table 2. Each unsmoothed maser spectrum can be seen in Appendix B, and a peak intensity map is presented in Appendix C. Appendices are available online.

Masers were identified by visual inspection of the data

by analysing various binned versions of the cube, such as 0.4, 0.6, 0.8, 1.0 and 2.0 km s^{-1} bins. This is effective at highlighting weak but broad maser emission; see for example G330.83+0.18 in Appendix B (available online). Any peak of emission exceeding 3σ in the various binned cubes with at least two adjacent channels of 2σ was considered for candidacy. The position of each maser reflects the brightest pixel within the neighbourhood of bright maser pixels. We compared the velocity of weaker maser candidates with CS and SiO $v = 0$ emission at the same location to strengthen their candidacy. In future work, we will re-observe each maser candidate to greater sensitivity and spatial resolution to confirm (or otherwise) its existence. The velocity range of each maser is determined by a 1.5σ cutoff in intensity from the peak velocity. As the channel resolution is approximately 0.2 km s^{-1}, velocities are specified to 0.1 km s^{-1}. All flux densities are specified with two significant figures. Intrinsic variation of masers along with calibration uncertainties place peak flux density errors within 20 per cent.

Using the program supplied by Reid et al. (2009), kinematic distances have been calculated and are included for each maser in Table 2. Parameters used for determining revised velocities and kinematic distances were taken from Green & McClure-Griffiths (2011), and the V_{LSR} uncertainty from Voronkov et al. (2014): $\Theta_0 = 246$ km s^{-1}, $R_\odot = 8.4$ kpc, $U_\odot = 11.1$ km s^{-1}, $V_\odot = 12.2$ km s^{-1}, $W_\odot = 7.25$ km s^{-1}, $U_s = 0$ km s^{-1}, $V_s = -15.0$ km s^{-1}, $W_s = 0$ km s^{-1}, $\sigma(V_{LSR}) = 3.32$ km s^{-1}. All distances are assumed to be kinematically "near", unless the distance prescribed by Green & McClure-Griffiths (2011) is "far".
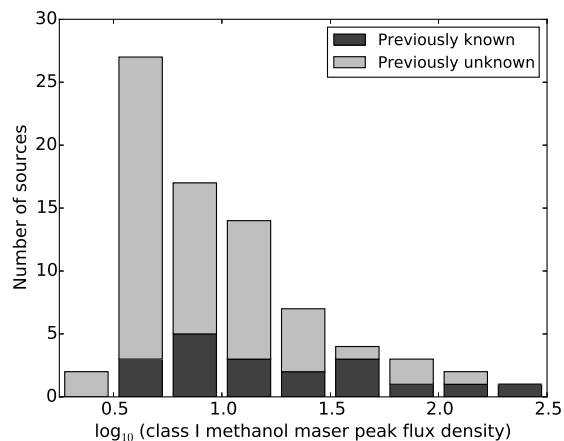

Figure 5: A stacked histogram of known and new class I CH$_3$OH maser peak flux densities. Previously known masers have a near even spread of flux densities, but the new MALT-45 population favours the weaker bins.

Table 2. Properties of detected MALT-45 class I CH_3OH maser emission. Each maser was detected within a 64 MHz zoom window. The first column lists the source name, derived from Galactic coordinates of the brightest peak. The second and third columns give the coordinates of the maser. The fourth column density lists the source peak flux density. The fifth column lists the RMS noise level of the peak. The sixth and seventh columns list the velocity range of maser emission, within a 1.5σ cutoff. The eight column lists the velocity at the peak. The ninth column lists kinematic distance calculated, based on position and peak velocity. The tenth and eleventh columns list the errors for the kinematic distance. The twelfth and thirteenth columns list the integrated intensity of CS (1–0) and SiO (1–0) $v = 0$ at the brightest peak. The fourteenth column gives additional remarks, mentioned in the footnotes[1]. The fifteenth column lists associations with other masers and EGOs, and is detailed in the footnotes[2]. Association is credited for any presence within 60 arcsec of the class I CH_3OH maser peak position. All velocities are specified to $0.1\,km\,s^{-1}$, and all flux densities are specified to two significant figures. Kinematic distances are derived using the kinematic distance model of Reid et al. (2009). All distances are assumed to be kinematically "near", unless labelled otherwise.

Source name	RA (J2000) (h m s)	Dec. (J2000) (° ′ ″)	Peak flux density (Jy)	RMS noise level	Velocity (km s⁻¹) Min.	Max.	Peak	Kinematic distance (kpc)	Distance error (kpc)		Integrated intensity (K km s⁻¹) CS	SiO	Remarks[1]	Other masers and EGOs[2]
G330.30−0.39	16 07 37.8	-52 30 52.1	4.4	4.9	-80.8	-79.5	-80.6	4.90	0.16	-0.16	3.1			W
G330.67−0.40	16 09 31.2	-52 16 03.9	5.3	5.6	-65.9	-64.6	-65.0	4.16	0.15	-0.15	2.5			
G330.78+0.24	16 07 12.8	-51 43 03.4	3.7	4.3	-43.8	-43.1	-43.4	3.12	0.17	-0.17	1.2			
G330.83+0.18	16 07 41.1	-51 43 48.0	3.1	3.8	-82.3	-79.7	-82.0	4.95	0.16	-0.16				
G330.87−0.36	16 10 16.6	-52 05 54.3	10	15	-67.0	-58.0	-61.4	4.00	0.15	-0.16	8.0	0.42	C	
G330.88−0.38	16 10 22.3	-52 06 28.1	7.8	10	-67.4	-58.0	-65.5	4.19	0.15	-0.15	8.6	0.56	C	MWSCG
G330.92−0.41	16 10 44.3	-52 06 04.0	28	33	-44.0	-41.0	-42.7	3.09	0.17	-0.17	1.4			
G330.93−0.26	16 10 06.9	-51 59 07.3	5.0	5.9	-91.4	-89.3	-89.9	5.33	0.17	-0.16	1.4			
G330.95−0.18	16 09 53.1	-51 54 57.9	4.0	4.7	-94.8	-86.7	-87.6	5.21	0.16	-0.16	9.6	1.4		MWCG
G331.13−0.48	16 12 00.3	-52 00 38.5	5.6	7.5	-69.1	-66.7	-68.0	4.30	0.15	-0.15	5.3	0.15		
G331.13−0.50	16 12 05.9	-52 01 33.3	8.6	11	-68.7	-67.8	-68.2	4.31	0.15	-0.15	4.5			
G331.13−0.25	16 11 00.7	-51 50 24.8	71	88	-92.9	-82.5	-91.4	5.39	0.17	-0.16	4.4	0.49	SVE	MWCG
G331.13+0.15	16 09 15.5	-51 33 08.1	68	60	-79.1	-74.6	-75.7	4.65	0.15	-0.15	1.2			MW
G331.21+0.10	16 09 52.2	-51 32 18.6	3.5	3.3	-67.8	-67.0	-67.4	4.27	0.15	-0.15				
G331.29−0.20	16 11 31.3	-51 41 54.8	15	20	-95.7	-85.0	-89.5	5.29	0.16	-0.16	3.7	0.17		MWC
G331.34−0.35	16 12 27.4	-51 46 26.9	32	37	-67.2	-65.0	-65.9	4.21	0.15	-0.15	2.1		SVE	MWCG
G331.36−0.02	16 11 06.4	-51 31 09.7	4.7	5.8	-84.6	-84.2	-84.4	5.05	0.16	-0.15				
G331.37−0.40	16 12 48.9	-51 47 26.2	5.9	7.3	-65.9	-65.0	-65.3	4.18	0.15	-0.15	1.6		C	G
G331.37−0.13	16 11 39.5	-51 35 35.3	3.7	4.5	-89.5	-88.8	-89.3	5.28	0.16	-0.16	1.6			
G331.39+0.15	16 10 28.7	-51 22 37.6	6.5	5.8	-46.5	-45.5	-45.9	3.26	0.16	-0.17	2.5	0.19		
G331.41−0.17	16 11 57.8	-51 35 40.6	4.9	6.6	-86.3	-84.8	-85.2	5.08	0.16	-0.15	2.7			
G331.44−0.19	16 12 11.4	-51 35 24.1	14	18	-92.5	-86.3	-88.2	9.53	0.16	-0.16	2.3	0.25	VF	MWC
G331.50−0.08	16 12 00.6	-51 27 44.3	38	49	-92.7	-86.7	-89.3	5.27	0.16	-0.16	4.1	0.14	P3	
G331.50−0.10	16 12 08.2	-51 29 01.0	11	14	-101.8	-86.1	-87.1	5.17	0.16	-0.15	6.5	0.31		WSC
G331.52−0.08	16 12 06.3	-51 27 35.5	20	18	-94.0	-88.0	-90.4	5.33	0.16	-0.16	5.8	0.13	P1	
G331.54−0.10	16 12 15.4	-51 27 17.1	77	77	-94.2	-89.1	-92.3	5.42	0.17	-0.16	7.4	0.29	P2	
G331.55−0.07	16 12 10.1	-51 25 39.9	4.9	5.3	-92.9	-86.3	-89.1	5.26	0.16	-0.16	4.9	0.15		MC
G331.56−0.12	16 12 26.8	-51 27 20.4	14	16	-104.8	-98.2	-101.0	5.87	0.19	-0.18	2.9			MWC
G331.72−0.20	16 13 33.1	-51 24 28.0	4.1	3.8	-47.2	-46.8	-47.0	3.32	0.16	-0.17	2.0			
G331.86−0.13	16 13 54.0	-51 15 32.1	5.6	6.5	-51.4	-49.5	-50.2	3.48	0.16	-0.16	2.6	0.44		
G331.88+0.06	16 13 11.6	-51 06 19.8	10	13	-90.1	-85.9	-89.3	5.26	0.16	-0.15	2.4	0.45		
G331.92−0.08	16 13 58.2	-51 10 46.7	5.8	6.4	-52.7	-51.6	-52.1	3.57	0.16	-0.16	1.5			
G332.09−0.42	16 16 13.7	-51 18 30.7	17	21	-59.5	-55.5	-56.1	3.76	0.15	-0.16	3.6			MW
G332.24−0.05	16 15 18.1	-50 56 03.2	140	180	-51.2	-45.9	-49.3	3.44	0.16	-0.16	3.4	0.32		
G332.30−0.09	16 15 43.9	-50 55 57.8	41	37	-52.5	-45.9	-49.9	3.47	0.16	-0.16	3.0		VE	MWG
G332.32+0.18	16 14 42.0	-50 42 50.2	9.3	11	-51.0	-48.0	-48.5	3.40	0.16	-0.16	1.2			W
G332.36−0.11	16 16 08.8	-50 53 55.2	9.8	12	-51.2	-49.9	-50.6	3.51	0.16	-0.16	1.7		C	MWCG
G332.59+0.15	16 16 01.3	-50 33 12.6	3.4	4.0	-43.6	-42.5	-42.7	11.79	0.17	-0.17			CF	MG
G332.60−0.17	16 17 28.1	-50 46 21.2	15	18	-47.6	-45.5	-46.1	3.29	0.16	-0.17	2.2		V	MWG
G332.72−0.05	16 17 27.9	-50 36 16.5	6.4	7.3	-41.0	-39.1	-40.4	3.01	0.17	-0.17				
G333.00−0.43	16 20 27.1	-50 40 58.3	6.6	9.8	-57.2	-56.1	-56.7	3.80	0.15	-0.15	4.8			W
G333.02−0.06	16 18 55.5	-50 24 04.3	6.8	7.9	-41.7	-39.7	-41.2	3.06	0.17	-0.17	1.2		E	MW
G333.03−0.02	16 18 44.6	-50 21 56.0	5.6	7.0	-42.9	-42.1	-42.5	3.12	0.17	-0.17				M
G333.07−0.44	16 20 48.4	-50 38 41.3	2.7	3.2	-55.3	-54.8	-54.8	3.72	0.15	-0.16	6.5	0.20		MW
G333.07−0.40	16 20 37.3	-50 36 33.5	4.1	4.6	-54.4	-52.7	-52.9	3.63	0.15	-0.16	4.2	0.21		
G333.10−0.51	16 21 15.1	-50 39 45.6	14	8.1	-58.9	-57.0	-57.6	3.85	0.15	-0.15	4.2			M
G333.13−0.44	16 21 04.0	-50 35 52.0	120	150	-57.2	-45.5	-50.2	3.50	0.16	-0.16	11	0.64	SVE P2	MWC
G333.14−0.42	16 21 01.8	-50 34 27.1	16	18	-56.7	-45.9	-56.3	3.79	0.15	-0.15	10	0.51	P1	W
G333.16−0.10	16 19 43.4	-50 19 43.0	5.6	7.7	-92.9	-91.2	-91.8	5.33	0.15	-0.14	1.3		E	M
G333.18−0.09	16 19 45.7	-50 18 18.3	5.6	7.1	-88.4	-85.7	-87.1	5.13	0.14	-0.14	1.7		E	MG
G333.22−0.40	16 21 18.6	-50 30 23.5	17	19	-55.3	-51.0	-51.9	3.59	0.15	-0.16	2.7			
G333.23−0.06	16 19 50.3	-50 15 28.9	250	310	-92.3	-84.4	-87.6	5.15	0.14	-0.14	1.0	0.25	SVE	MWSC
G333.24+0.02	16 19 29.5	-50 11 23.5	3.9	5.4	-69.5	-67.8	-69.3	4.37	0.14	-0.14	1.4			
G333.29−0.38	16 21 29.7	-50 26 30.3	5.4	6.3	-53.6	-50.6	-52.3	3.61	0.15	-0.16	11	0.27		
G333.30−0.35	16 21 25.3	-50 25 05.4	3.5	3.6	-53.1	-49.5	-50.8	3.54	0.16	-0.16	9.8	0.18		
G333.31+0.10	16 19 28.7	-50 04 50.9	7.7	13	-50.6	-43.8	-45.3	11.74	0.17	-0.16	2.1	0.12	ECF	MWG
G333.33−0.36	16 21 36.4	-50 23 40.6	22	22	-53.8	-49.5	-52.1	3.60	0.15	-0.16	6.0	0.27		
G333.37−0.20	16 21 04.4	-50 15 21.6	13	16	-62.3	-57.6	-61.6	4.03	0.15	-0.15				W
G333.39+0.02	16 20 10.6	-50 04 53.7	4.1	6.5	-72.9	-69.7	-70.6	10.60	0.14	-0.14			F	MWC
G333.47−0.16	16 21 22.1	-50 09 42.5	21	23	-46.1	-41.4	-43.4	3.18	0.16	-0.17	3.6		E	MWCG
G333.50+0.15	16 20 07.6	-49 55 10.1	3.5	5.9	-114.4	-112.0	-112.9	6.35	0.21	-0.19				
G333.52−0.27	16 22 01.9	-50 12 11.2	6.4	8.7	-51.2	-50.2	-50.6	3.53	0.16	-0.16	3.5			
G333.56−0.30	16 22 19.6	-50 11 28.6	7.8	11	-48.0	-45.9	-46.5	3.33	0.16	-0.17	2.4			
G333.56−0.02	16 21 09.0	-49 59 48.3	54	63	-41.7	-39.1	-40.2	12.02	0.17	-0.17	1.8		EF	M
G333.57+0.03	16 20 55.9	-49 57 19.4	6.2	6.4	-85.7	-84.8	-85.0	5.04	0.14	-0.14	0.95			
G333.59−0.21	16 22 08.5	-50 06 31.7	26	34	-51.2	-47.6	-49.7	3.49	0.16	-0.16	11	0.31	SV	WSC
G333.70−0.20	16 22 29.4	-50 01 23.8	4.4	6.1	-51.2	-50.8	-51.0	3.55	0.16	-0.16	2.4			
G333.71−0.12	16 22 12.8	-49 57 20.1	6.6	6.9	-32.3	-31.2	-31.9	2.58	0.18	-0.19				
G333.77−0.01	16 22 00.7	-49 50 26.5	16	20	-90.5	-88.8	-89.5	5.22	0.14	-0.14	2.3			
G333.77−0.25	16 23 03.5	-50 00 51.0	6.4	8.0	-50.2	-49.3	-49.5	3.49	0.16	-0.16	2.4	0.12		
G333.82−0.30	16 23 28.8	-50 00 39.2	19	24	-49.5	-47.8	-48.5	3.44	0.16	-0.16	1.3			
G333.90−0.10	16 22 57.7	-49 48 39.2	3.4	4.1	-65.3	-62.9	-64.4	10.92	0.15	-0.14			F	M
G333.94−0.14	16 23 17.4	-49 48 38.4	4.6	4.9	-43.1	-42.3	-42.3	3.14	0.17	-0.17				MW
G333.98+0.07	16 22 34.6	-49 37 52.8	4.5	5.7	-60.8	-58.0	-58.4	3.90	0.15	-0.15				
G334.03−0.04	16 23 15.0	-49 40 51.7	11	14	-84.8	-84.0	-84.4	5.01	0.14	-0.14	2.0			
G334.64+0.44	16 23 50.4	-48 54 08.7	5.7	6.4	-67.2	-66.5	-66.5	4.27	0.14	-0.14	2.2			
G334.74+0.51	16 23 56.6	-48 47 03.7	18	6.7	-65.5	-61.4	-61.4	4.05	0.14	-0.15	1.1	0.17		

[1]S - 44 GHz detection from Slysh et al. (1994); V - 95 GHz detection from Val'tts et al. (2000); E - 95 GHz detection from Ellingsen (2005); C - 95 GHz detection from Chen et al. (2011); P - indicates a blended spectrum of emission. P1 contains a strong peak of emission at a spatially distinct position, with a different velocity to nearby strong masers (but not as strong as the neighbour), P2 is the strong neighbour, and P3 is the next strongest neighbour; F - this maser has been labelled as being kinematically "far", due to a class II CH_3OH maser being labeled as such by Green & McClure-Griffiths (2011). Note that a source without a S, V, E or C remark is a new detection. [2]M - presence of a 6.7 GHz class II methanol maser (Caswell et al. 2011); W - presence of a 22 GHz H_2O maser (Walsh et al. 2011; Breen et al. 2010); G - presence of an EGO classified by Cyganowski et al. (2008); S - presence of a 1612 OH maser (Sevenster et al. 1997); C - presence of a 1665 or 1667 MHz OH maser (Caswell et al. 1998).

Table 3. Properties of detected MALT-45 SiO (1–0) maser emission. Each maser was detected within a 64 MHz zoom window. The first column lists the source name, derived from Galactic coordinates of the brightest peak. The second and third columns give the coordinates of the maser. Columns four through fifteen are categorised into $v = 1$, $v = 2$ and $v = 3$. For each category, there are four columns, listing the peak flux density within this vibrational mode (if detected), and the minimum, maximum and peak velocities. The sixteenth column lists the RMS noise level, which indicates the most statistically significant maser peak detected among the three modes. The seventeenth column lists the kinematic distance calculated, based on position and peak velocity. The eighteenth and nineteenth columns list the errors for the kinematic distance. The twentieth column gives additional remarks, clarified in the footnotes[1]. If data are not available in one of the lines for a source, it was not detected by MALT-45. Velocity ranges (between minimum and maximum) are determined by a 1.5σ cutoff. All velocities are specified to $0.1\,\mathrm{km\,s^{-1}}$, and all flux densities are specified to two significant figures. Association is credited if the source position is within 30 arcsec of the peak SiO maser position. Kinematic distances are derived using the kinematic distance model of Reid et al. (2009). All distances are assumed to be kinematically "near", except for G330.14−0.39, G331.08+0.17, G332.40−0.33 and G334.20+0.22; when assumed to be near, unphysical distances and errors are generated.

Source name	RA (J2000) (h m s)	Dec. (J2000) (° ′ ″)	SiO $v = 1$ properties Peak flux density (Jy)	Velocity Min. (km s⁻¹)	Velocity Max. (km s⁻¹)	Peak	SiO $v = 2$ properties Peak flux density (Jy)	Velocity Min. (km s⁻¹)	Velocity Max. (km s⁻¹)	Peak	SiO $v = 3$ properties Peak flux density (Jy)	Velocity Min. (km s⁻¹)	Velocity Max. (km s⁻¹)	Peak	RMS noise level	Kinematic distance (kpc)	Distance error (kpc)		Remarks[1]
G330.12−0.31	16 06 24.3	-52 34 33.5					3.5	-65.8	-61.2	-61.4					4.8	3.46	0.23	-0.23	
G330.14−0.39	16 06 52.6	-52 37 04.9	6.3	-2.6	4.5	3.5	7.5	-3.0	5.5	3.6					11	5.05	0.45	-0.41	W
G330.47+0.03	16 06 36.7	-52 05 15.6	23	-59.5	-48.3	-53.7	13	-59.7	-51.6	-54.4	2.5	-56	-52.7	-53.8	26	3.12	0.24	-0.24	W
G330.51+0.01	16 06 53.2	-52 04 19.6	11	-13.7	-9.8	-12.2	19	-15.5	-10.2	-12.8					19	0.76	0.34	-0.36	
G330.55+0.15	16 06 28.1	-51 56 41.6	4.0	-68.7	-67.8	-68.0	2.7	-69.7	-68	-69.3					4.9	3.80	0.22	-0.23	
G330.75+0.20	16 07 15.2	-51 46 25.6	2.9	-66.1	-65.2	-65.8	2.7	-64.0	-67.1	-63.8					3.8	3.63	0.22	-0.23	
G330.85−0.44	16 10 29.3	-52 10 34.9	3.4	-32.0	-30.7	-31.7									4.3	1.98	0.28	-0.29	W
G331.08+0.17	16 08 55.8	-51 34 14.6	4.9	-6.1	-3.9	-5.2									7.3	4.45	0.40	-0.37	
G331.13−0.27	16 11 06.2	-51 51 19.7	4.6	-31.5	-30.0	-30.7	4.7	-32.1	-30.3	-31.0					7.7	1.94	0.28	-0.29	
G331.21+0.25	16 09 10.8	-51 25 19.1	2.9	-36.7	-34.6	-36.1	3.0	-37.1	-36.0	-36.3					4.4	2.24	0.27	-0.28	
G331.24−0.02	16 10 32.2	-51 36 05.6	2.7	-90.0	-89.1	-89.1									3.2	4.69	0.22	-0.21	
G331.48−0.03	16 11 43.7	-51 26 46.0	7.0	-69.5	-66.3	-68.0	5.7	-69.7	-62.9	-68.4					9.1	3.80	0.22	-0.22	
G331.58+0.07	16 11 44.5	-51 18 06.2	2.7	-33.7	-32.4	-32.8									3.4	2.06	0.28	-0.29	
G331.60−0.14	16 12 42.8	-51 26 42.7	2.8	-96.5	-93.9	-95.6	7.8	-97.3	-94.0	-96.0	2.7	-96.3	-94.6	-95.9	9.9	4.98	0.22	-0.21	CS
G331.65−0.25	16 13 28.8	-51 29 34.6	4.4	-38.3	-34.8	-36.5	3.5	-39.1	-35.4	-36.5					5.7	2.27	0.27	-0.28	S
G331.70−0.03	16 12 43.5	-51 17 20.4	3.1	-26.1	-25.2	-25.4	1.7	-25.5	-24.7	-25.3					3.6	1.63	0.30	-0.31	
G331.72+0.45	16 10 43.2	-50 55 38.7	4.2	18.9	21.1	20.0	3.6	18.2	21.3	19.8					4.9	6.97	0.62	-0.57	S
G331.76−0.33	16 14 19.0	-51 28 22.3	28	-36.1	-23.9	-29.1	24	-34.1	-24.2	-29.7	3.6	-30.4	-24.5	-25.6	40	1.79	0.29	-0.30	W
G331.95+0.08	16 13 23.5	-51 02 50.8	2.8	-102.8	-98.4	-101.9	2.5	-99.7	-102.5	-99.7					4.2	5.19	0.22	-0.21	
G331.96−0.24	16 14 52.6	-51 16 07.2	3.0	-81.5	-80.2	-80.8									3.9	4.35	0.21	-0.21	W
G331.99−0.04	16 14 05.7	-51 06 12.7	2.9	-99.1	-97.1	-98.0	2.8	-98.2	-98.6	-98.2					3.9	5.07	0.21	-0.21	
G332.14−0.51	16 16 52.0	-51 20 23.1	5.1	-36.7	-35.2	-36.5	6.9	-36.9	-35.4	-36.3					4.5	2.28	0.27	-0.28	
G332.22+0.36	16 13 25.5	-50 39 30.7	3.4	-121.2	-120.6	-121.0	2.1	-122.2	-122.7	-122.2					4.4	6.17	0.32	-0.27	
G332.30+0.44	16 13 27.9	-50 32 16.3	6.2	-56.3	-54.1	-55.4	3.6	-56.4	-54.4	-55.3					8.4	3.24	0.23	-0.24	
G332.40−0.33	16 17 16.5	-51 01 21.2					2.7	-7.4	-5.0	-5.6					3.8	4.61	0.41	-0.38	
G332.83+0.19	16 16 57.1	-50 21 10.2	4.8	-34.3	-31.7	-33.7									5.1	2.15	0.27	-0.29	
G332.90−0.37	16 19 41.3	-50 42 31.2	2.2	-102.1	-99.7	-101.0	3.4	-101.7	-102.5	-101.7					4.9	5.20	0.21	-0.20	
G333.06−0.10	16 19 14.4	-50 24 16.6	4.4	-48.9	-43.3	-45.4	6.8	-48.5	-43.7	-45.7					9.5	2.79	0.25	-0.26	W
G333.44−0.07	16 20 49.1	-50 06 52.0	3.3	-96.9	-95.4	-96.3	2.7	-97.1	-98.6	-97.1					4.2	5.00	0.20	-0.20	
G333.46−0.34	16 22 06.3	-50 17 29.4	4.3	-63.0	-56.7	-58.5	4.3	-64.7	-58.6	-64.3					5.4	3.55	0.22	-0.23	
G333.53+0.41	16 19 06.9	-49 42 21.9	3.3	-145.1	-144.7	-144.9									4.0	7.52	0.77	-0.77	
G333.60−0.49	16 23 21.6	-50 18 09.7	4.1	-16.1	-15.0	-15.7	3.0	-16.3	-15.7	-15.9					4.8	1.06	0.34	-0.36	
G333.64−0.37	16 22 59.3	-50 11 06.3	4.1	-70.6	-67.8	-69.5	4.5	-70.8	-69.1	-70.2					6.3	3.93	0.21	-0.21	W
G333.72−0.39	16 23 25.8	-50 08 36.6	5.2	-44.3	-40.4	-43.3	5.0	-45.7	-41.5	-43.5					7.1	2.71	0.25	-0.26	
G333.78−0.36	16 23 35.6	-50 04 53.2	2.1	-93.4	-92.1	-92.4	1.6	-93.1	-92.7	-92.9					3.1	4.85	0.20	-0.20	
G333.90−0.09	16 22 56.6	-49 48 07.4	3.8	-126.0	-123.2	-123.9	4.0	-123.8	-122.9	-123.1					4.5	6.12	0.26	-0.23	S
G334.01−0.02	16 23 06.3	-49 40 30.9	3.3	-94.3	-93.0	-93.4	3.3	-95.5	-93.6	-93.8					3.9	4.89	0.19	-0.19	
G334.11−0.37	16 25 05.0	-49 50 58.6	3.9	-32.8	-30.9	-31.5									4.7	2.08	0.28	-0.30	
G334.20+0.22	16 22 49.6	-49 22 18.8	2.7	-7.4	-7.0	-7.2	2.8	-5.2	-7.4	-5.2					4.4	4.78	0.42	-0.39	
G334.35−0.36	16 26 03.3	-49 40 15.0	3.2	-22.8	-21.5	-22.6									4.1	1.54	0.31	-0.33	
G334.35+0.06	16 24 13.2	-49 22 24.8	3.8	-82.6	-81.9	-82.1									3.8	4.44	0.20	-0.20	
G334.41+0.22	16 23 44.6	-49 13 15.1	3.9	-32.8	-31.7	-32.2	3.0	-32.5	-32.1	-32.3					4.7	2.13	0.28	-0.30	
G334.49−0.37	16 26 41.1	-49 34 40.5	3.8	-9.8	-8.5	-9.1	2.7	-10.2	-8.9	-10.0					4.7	0.62	0.38	-0.41	
G334.61−0.43	16 27 29.9	-49 32 14.1	5.0	-139.5	-138.2	-138.8	3.3	-139.7	-138.9	-139.3					5.7	6.97	0.36	-0.36	
G334.68+0.44	16 23 57.9	-48 52 53.8	3.6	-96.9	-95.2	-95.2									3.8	4.96	0.19	-0.19	
G334.68+0.35	16 24 22.8	-48 56 34.8	4.0	-55.6	-55.2	-55.2	2.6	-55.9	-56.4	-55.9					4.4	3.34	0.23	-0.23	
G334.68+0.13	16 25 20.5	-49 05 30.2	5.1	-94.5	-89.1	-91.1	2.2	-93.4	-91.8	-92.5					6.1	4.83	0.19	-0.19	W

[1]C - presence of a 1665 MHz OH maser from Caswell et al. (1998); S - presence of a 1612 MHz OH maser from Sevenster et al. (1997); W - presence of a H_2O maser from Walsh et al. (2011, 2014).
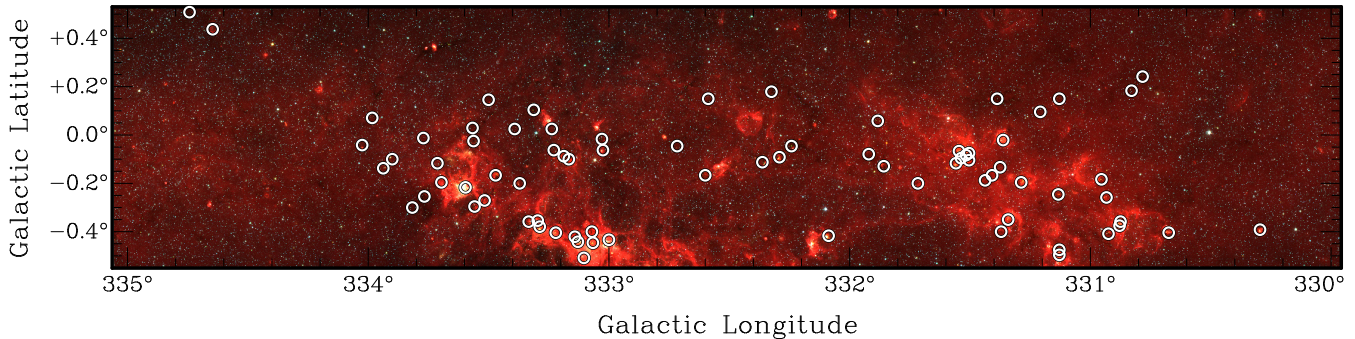
Figure 6: *Spitzer* GLIMPSE 3-colour (RGB = 3.6, 4.5 and 8.0 μm) image with MALT-45 positions of class I CH$_3$OH masers (circle symbols).
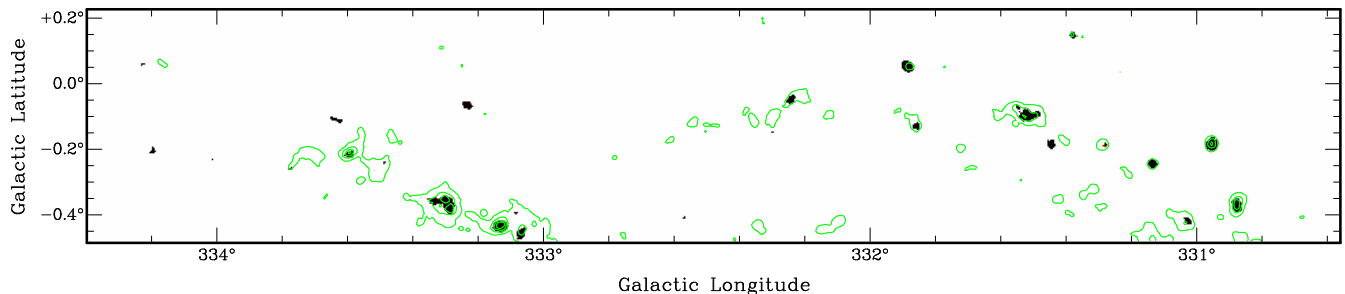

Figure 7: Auto-correlated map of SiO (1–0) $v = 0$, overlaid with CS (1–0) thermal emission contours. This image shows SiO emission at and above 0.04 K ($\sim$1.5σ). Contour levels are 14, 34, ...74 per cent of 2.62 K.

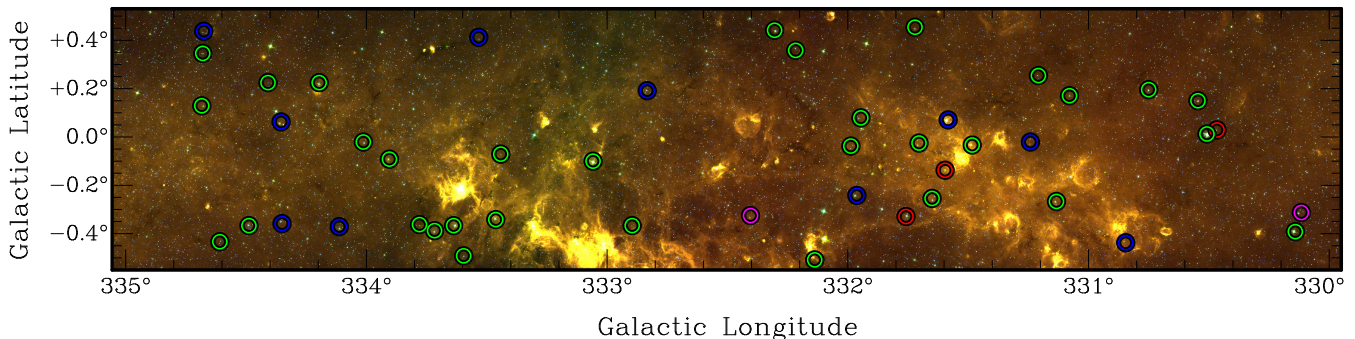Figure 8: *Spitzer* GLIMPSE 3-colour (RGB = 3.6, 5.8 and 8.0 μm) image with MALT-45 positions of detected SiO (1–0) $v = 1, 2, 3$ masers (circle symbols). The circles have been colour-coded by the vibrational modes within each region. Red: region containing $v = 1, 2, 3$ maser emission; green: $v = 1, 2$; blue: $v = 1$; magenta: $v = 2$.

The positions of class I CH$_3$OH masers have been compared with the published positions of class II CH$_3$OH, H$_2$O and OH masers to establish associations. When considering the maximum distance between masers that still constitute an association, we use 60 arcsec from the class I position as suitable for defining associations. Csengeri et al. (2014) analysed a large distribution of clumps associated with HMSF in their source sample, and find that all clumps have effective radii within 55 arcsec. Additionally, we note that increasing the maximum offset beyond 60 arcsec does not increase the number of unique associations. These findings suggest for our purposes that 60 arcsec is sufficient to group masers within a single star-forming region. We have chosen not to

define an association based on source distance or size, as it is difficult to implement across a wide range of objects, kinematic distances may be erroneous, and maser geometry may be wide-spread. An angle of 60 arcsec on the sky corresponds to approximately 1.5 pc at a distance of 5 kpc.

There are two targets where the spread of class I CH$_3$OH maser emission is large and these have been considered as two separate maser regions. The weaker masers (G331.52−0.08 and G333.14−0.42) near to each of these bright masers (G331.50−0.08 and G333.13−0.44) possess a distinct spectral velocity component and are sufficiently spatially offset to be considered a different site (54 and 87 arcsec, respectively). See the spectra in Appendix B (avail-
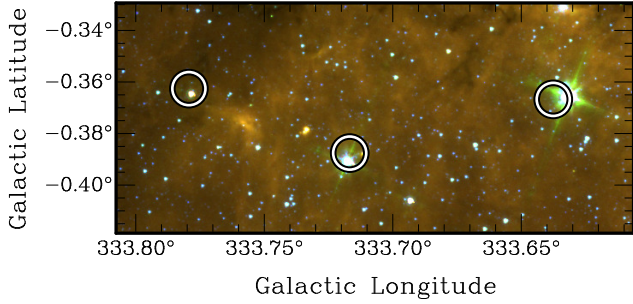
Figure 9. *Spitzer* GLIMPSE 3-colour (RGB = 3.6, 5.8 and 8.0 μm) image with examples of detected SiO masers towards infrared stars. Circles are centred on the peak position of maser emission, and are beam-sized (1 arcmin). All three of these SiO maser regions contain the $v = 1$ and $v = 2$ lines, but all other maser region variants have similar infrared colours.

able online). These sources are marked with a "P" in Table 2.

Integrated intensity values for CS and SiO $v = 0$ have been included for each maser, where possible, in Table 2. Emission was integrated $\pm 10\,\mathrm{km\,s^{-1}}$ from the peak velocity of the maser. Values were not included if the emission was not significant ($< 3\sigma$).

3.3 SiO (1–0) $v = 0$ thermal emission at 43.424 GHz

Extended SiO $v = 0$ emission is detected in some regions, as shown in Figure 7, which shows that SiO $v = 0$ emission tends to be associated with bright peaks of CS emission. Note that emission from the SiO $v = 0$ is typically weaker than for CS, hence the signal-to-noise is lower for this transition; Figure 7 shows all emission above 1.5σ. Discussion on the relation between class I CH$_3$OH masers and SiO $v = 0$ emission is contained in Section 4.3.

3.4 SiO (1–0) $v = 1, 2, 3$ masers at 43.122, 42.820 and 42.519 GHz

The vibrationally excited SiO (1–0) lines were detected towards 47 regions, as shown in Figure 8. The properties of each maser region are classified in Table 3. The search procedure for SiO masers was the same as with CH$_3$OH masers; they were identified by visual inspection of the data, and had velocities categorised by a 1.5σ cutoff from the peak velocity. Velocities are specified to $0.1\,\mathrm{km\,s^{-1}}$, and flux densities to two significant figures. Many masers have low signal-to-noise values, but are considered real detections based on their association in GLIMPSE, and simultaneous detection of emission in another SiO maser transition. The positions of SiO masers have been compared with OH and H$_2$O masers; see Table 3 and Section 4.7. CH$_3$OH maser species were searched at these positions, but none were found, implying that any class I CH$_3$OH maser emission associated with the SiO masers has a peak flux density <4.5 Jy. Peak intensity maps are presented in Appendix C, and each un-smoothed maser spectrum can be seen in Appendix D. Appendices are available online.

Figure 8 shows the locations of SiO masers detected by

MALT-45 with respect to infrared emission from GLIMPSE. All SiO masers are detected towards point-like, isolated sources that appear to be evolved stars, based on their infrared colours and lack of obvious associations with star formation, such as IRDCs or extended infrared emission. Figure 9 shows the relative locations of three SiO masers compared to infrared stars; these masers were chosen as they show various colours of infrared stars towards all SiO masers. It can be seen that the maser locations are not identical to the stars, but are within one beam. Therefore, we cannot conclusively argue that each SiO maser site is coincident with an evolved star, although the evidence we have suggests this is the case. Further higher spatial resolution observations of the maser sites will be able to demonstrate conclusively whether or not each SiO maser is associated with an evolved star.

Of the 47 SiO maser regions, 45 contain $v = 1$ emission, 37 contain $v = 2$, and only 3 have $v = 3$ emission. We have found no previously published data for any of these SiO masers and consider them all to be new detections. Some SiO maser regions have greater $v = 2$ emission than $v = 1$, and two have no detected emission $v = 1$; this is discussed further in Section 4.7. There are also 12 SiO maser regions with an associated OH or H$_2$O maser; see Section 4.7.

Parameters used in determining kinematic distances are the same as those found in Section 3.2, except for a more generous velocity uncertainty $\sigma(V_{LSR}) = 5.0\,\mathrm{km\,s^{-1}}$, and $V_s = 0\,\mathrm{km\,s^{-1}}$. Four masers are labelled at the far kinematic distance, because the position and errors for a near distance are unrealistic; see Table 3.

3.5 Survey completeness

By analysing the RMS noise values per pixel distributed across the MALT-45 region, we find that the noise levels may vary by up to a factor of three due to some data being flagged or insufficient time on the telescope to complete the observations. However, we determine that approximately 95 per cent are consistent with the values listed in Table 1, and only 5 per cent show RMS levels worse than these values. Thus, we assess that to first order the survey has uniform sensitivity and only a small fraction of the area has sensitivity poorer than nominal.

Tables 2 and 3 include the RMS value for each detected maser peak, which help to identify the completeness of the MALT-45 survey. We detect many masers at less than 5σ significance. However, we consider the survey complete at the 5σ level for 95 per cent of the survey area. This completeness limit is equivalent to 4.5 Jy for class I CH$_3$OH masers, and approximately 4.3 Jy for each SiO maser line.

4 DISCUSSION

4.1 Comparing CS (1–0) with HOPS NH$_3$ (1,1)

Figure 4 shows that NH$_3$ (1,1) from HOPS is closely correlated with bright CS (1–0) emission, but with prominent exceptions; examples include G330.30$-$0.40, G332.17$-$0.10 and G334.17+0.06. We calculate that MALT-45 is more sensitive to CS (1–0) emission than HOPS is to NH$_3$ (1,1) by a factor approximately 9, therefore CS without NH$_3$ in Figure
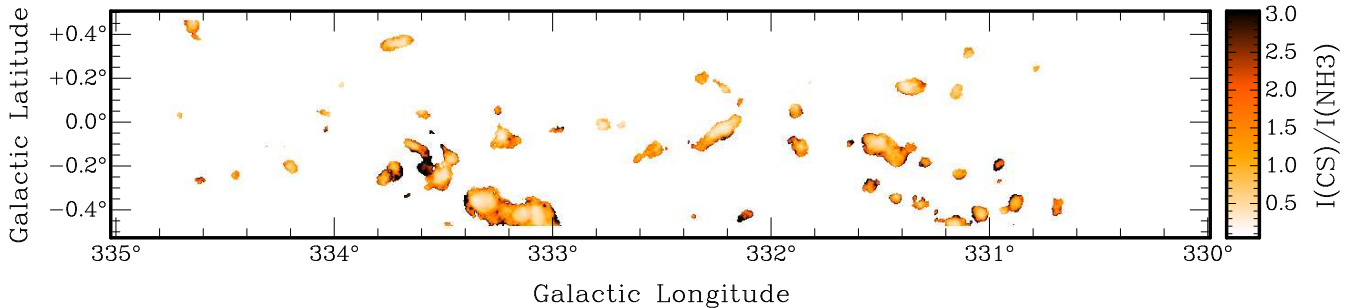
Figure 10. A ratio image of integrated MALT-45 CS (1–0) to HOPS NH$_3$ (1,1). The clumps visible here contain at least $0.5\,\mathrm{K\,km\,s^{-1}}$ of integrated NH$_3$ (1,1) emission. Most clumps have edge values around 2, and centres of clumps can have values as low as 0.4.

4 may be due to the superior sensitivity of MALT-45 over HOPS. However, it is also likely attributable to the phenomena described by Taylor et al. (1998), who reason that CS is an "early-type" star-forming molecule, tracing quiescent gas, while NH$_3$ is "late-type", associated with dense cores. For this reason, despite having a higher effective critical density, CS without NH$_3$ may be tracing molecular clouds before cold, dense cores have formed. Additionally, Bergin et al. (2001) and Tafalla et al. (2002) indicate that CS tends to deplete in core collapse. This means a relatively high abundance of NH$_3$ to CS should reflect a cold, dense core, which is a Taylor et al. (1998) "late-type" scenario. As results indicate later in this section, NH$_3$ is not persistent in even further developed stages of HMSF, as it is not detected or very faint. We distinguish "late-type" sources from these evolved sources through bolometric luminosities and the presences of infrared features, such as stars or H II regions.

We produced a map of the ratio between the integrated intensities of CS and NH$_3$ in order to highlight the differences between their distributions. Before performing the quotient of integrated intensity, the CS data were smoothed to the HOPS NH$_3$ resolution ($\sim$2 arcmin). We used a cutoff at $0.5\,\mathrm{Kkm\,s^{-1}}$ (3σ) of the less sensitive NH$_3$ data; CS data is $> 3\sigma$ everywhere NH$_3$ is $> 3\sigma$. Integration of emission was taken between -100 and $-40\,\mathrm{km\,s^{-1}}$, to eliminate subtle baseline effects which decrease the robustness of analysis; this velocity range is where most of the emission in this part of the Galaxy lies (see Figure 3 for the longitude-velocity plot). Quotients use units of main-beam temperature for both CS and NH$_3$. See Figure 10 for the full ratio map.

Moving inward from the clump edges, the CS/NH$_3$ ratio quickly changes. We observe the amount of both CS and NH$_3$ to increase, with the NH$_3$ intensity increasing more "quickly". Edge values are mostly about 2, while clump centres are usually between 1 and 0.5, but can be as low as 0.4.

We now discuss the ratio map qualitatively, reserving radiative transfer modelling for future work. In almost every clump, the centre is dominated by NH$_3$ over CS. This could be due to any or a combination of enhanced NH$_3$, depleted CS, or both species being enhanced but CS becoming optically thick. The hyperfine line structure of NH$_3$ means that it remains optically thin at higher column densities than CS. To test for optically thick CS, we compared CS with MALT-45 C^{34}S.

We conducted the analysis of CS against C^{34}S in a similar manner to that of CS against NH$_3$. Both integrated maps

were smoothed to the same resolution, the velocity range of integration was -100 to $-40\,\mathrm{km\,s^{-1}}$, and emission was limited to detectable C^{34}S ($0.15\,\mathrm{K\,km\,s^{-1}}$). A preliminary analysis of the C^{34}S data was undertaken only to investigate the CS optical depth within these clumps.

Figure 11 shows contours of the ratio of C^{34}S/CS against GLIMPSE, with contours of CS/NH$_3$. Progressively higher levels of C^{34}S/CS indicate CS self-absorption, but appear to be slightly offset from the lowest CS/NH$_3$ ratios. This implies that the relatively fainter CS emission in the presence of an abundance of NH$_3$ is due to both depletion and optical thickness. Additionally, the higher ratios of C^{34}S/CS appear to be associated with bright infrared emission, and correlate well thermal SiO emission. We speculate that high C^{34}S/CS ratios may be due to high CS optical depth as a result of high CS relative abundance in the presence of an outflow or shocked gas. C^{34}S is not detected in other regions of these clumps; aside from having poor signal-to-noise, this is likely due to the isotopologue depleting similar to CS, and emission is only apparent in hotter, shocked regions where these molecules have been released into the gas phase.

A similar analysis to the one we have conducted was performed in Tafalla et al. (2004) towards two cold, dense cores. Their results indicate significant depletion of CS and C^{34}S towards the core centres, while NH$_3$ peaks in abundance. We have not undertaken a detailed analysis of the temperature or mass of the MALT-45 molecular gas clumps in this paper; this will be investigated in a future publication focusing on the CS emission. In future work, we will present radiative transfer modelling (including depletion, time-dependant chemistry and the relative sensitivity limits of the various surveys) of the dust, CS and NH$_3$ emission to quantitatively understand the physical reason for these effects.

The following subsections briefly discuss three unusual clumps, which have the largest CS/NH$_3$ ratios.

4.1.1 G330.95−0.19

This source is one of the brightest in CS across the MALT-45 survey region (peak of 1.5 K), and is the brightest in thermal SiO emission (peak of 0.17 K). The source also contains all the common star formation region masers: class I and II CH$_3$OH, H$_2$O and OH. The CS spectrum has a broad profile of $\sim$10 km s^{-1} FWHM, possibly due to a powerful molecular
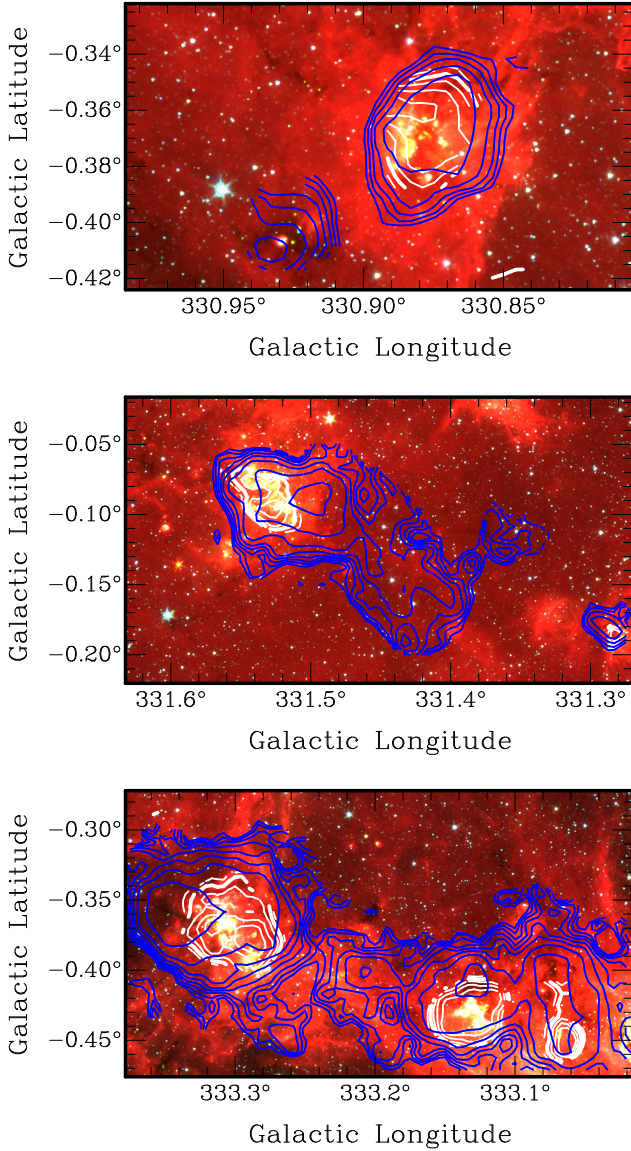
Figure 11. Examples of significant $C^{34}S$/CS ratios within CS/NH$_3$ clumps. *Spitzer* GLIMPSE 3-colour (RGB = 3.6, 4.5 and 8.0 μm) image with contours of I($C^{34}S$)/I(CS) (white) and contours of I(CS)/I(NH$_3$) (blue). I($C^{34}S$)/I(CS) contour levels are 0.08, 0.10, ...0.16, and I(CS)/I(NH$_3$) contour levels are 0.3, 0.5, ...1.9. Note that contour levels for I(CS)/I(NH$_3$) move from large to small, outside-in. The lowest CS/NH$_3$ and highest $C^{34}S$/CS ratios appear to be slightly offset. High $C^{34}S$/CS ratios appear to occur with bright infrared emission; this is likely due to $C^{34}S$ is only detectable where the overall CS abundance is enhanced in hotter, shocked regions where these molecules have been released into the gas phase.

outflow. A strong outflow would not be surprising given the strength of the thermal SiO detected, relative to all other SiO sources in MALT-45.

Garay et al. (2010) have targeted this source which has a high IRAS far-infrared luminosity, as well as detection of CS (2–1) by Bronfman, Nyman & May (1996). Garay et al. (2010) present data for SiO (2–1) and note that of the four sources they discuss, this source is brightest in SiO, and conclude that an outflow is present due to the spectral

profiles of CS and SiO. Garay et al. (2010) also discuss the requirement of OB stars to produce the ionised gas seen in other observations. The evolved nature of the source is the likely reason for the faint NH$_3$, because it is being destroyed or dispersed by outflows or young stellar objects.

4.1.2   *G332.10−0.42*

The CS/NH$_3$ ratio of this source is approximately 3. Of the three unusual sources discussed in this section, this is the only one without detected thermal SiO emission. A small region (∼30 arcsec) of the clump has a constant $C^{34}S$/CS ratio of 0.08, and is coincident with a H$_2$O and class II CH$_3$OH maser, as well as what appears to be a star in GLIMPSE. A new class I CH$_3$OH maser is detected by MALT-45, but is slightly offset from this position (∼30 arcsec).

This source has been targeted by Ilee et al. (2013) to determine disc properties through CO observations, and is listed with a very high bolometric luminosity (1.8×10^5 L$_\odot$). The Red MSX Source (RMS; Lumsden et al. 2013) survey also lists a *K*-band magnitude of 5.9. These values suggest that the source is not embedded. As a star is visible in GLIMPSE and the source is not embedded, it may be assumed that the star (and the region) are post star-forming. However, we are confident that the associated star is not evolved (beyond the main-sequence), as a near-infrared (NIR) spectrum of the source contains Brγ, indicating the presence of an H II region. The spectrum is taken from the RMS survey, although the data remain unpublished; Cooper et al. (2013) present detailed analysis of the NIR spectroscopy, but note that it does not cover this specific source. We conclude that this source is somewhat evolved because of its exposure from natal clouds, but is premain-sequence because of the class II CH$_3$OH maser emission. Again, the evolved nature of this region is the likely reason for the relatively faint NH$_3$.

4.1.3   *G333.60−0.20*

This region is the brightest H II region within the MALT-45 survey, and appears to harbour evolved sources. $C^{34}S$ emission is detected within this source, and the $C^{34}S$/CS ratio varies from 0.09 to 0.14. Thermal SiO emission is also detected towards the source. As well as a previously known class I CH$_3$OH maser, this region is associated with 1612-, 1665- and 1667-MHz OH masers (Sevenster et al. 1997; Caswell et al. 1998), and many H$_2$O masers from HOPS (Walsh et al. 2014). The peak velocity of the class I CH$_3$OH maser is $-49.7\,\mathrm{km\,s^{-1}}$, $-51\,\mathrm{km\,s^{-1}}$ for OH, and -75.5 to $-43.1\,\mathrm{km\,s^{-1}}$ for the H$_2$O masers. MALT-45 CS also has a double-peak profile in this region; a strong, broad peak is associated with $-48.1\,\mathrm{km\,s^{-1}}$ and a weaker one at $-89.8\,\mathrm{km\,s^{-1}}$, both at the same position ($16^h22^m06^s$, $-50°06'17''$ J2000).

Fujiyoshi et al. (2006) conducted observations of H90α towards this source, which also reveal two peaks of emission, and reason that it contains many O-type stars. The peak velocity of each H90α component varies greatly over the region, from -78.5 to $-52.9\,\mathrm{km\,s^{-1}}$ and -42.8 to $-22.8\,\mathrm{km\,s^{-1}}$, where the second peak is weaker and not present across the observed area. Note that the position of
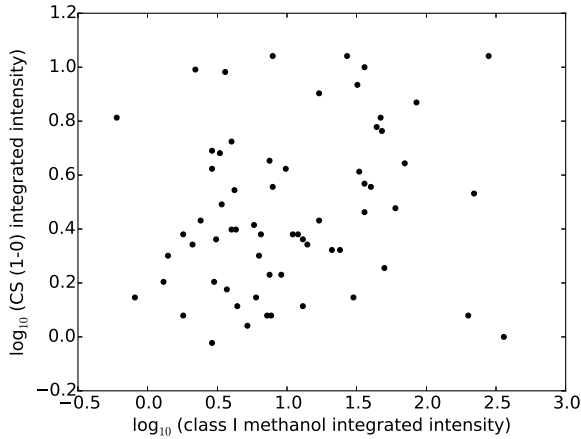
Figure 12. A log-log scatter plot of class I CH_3OH and CS integrated intensities. Units of integrated intensity are $Jy\,km\,s^{-1}$ for class I CH_3OH, and $K\,km\,s^{-1}$ for CS. There is no significant correlation observed in either subpopulation, or the total population.
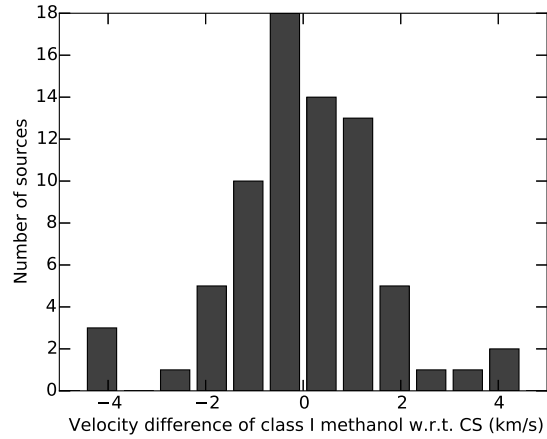

Figure 13. The distribution of velocity offsets between the peak velocity of class I CH_3OH and CS (1–0). The bin size was chosen to be $0.75\,km\,s^{-1}$. The histogram is approximated by a Gaussian with a mean velocity $0\pm0.2\,km\,s^{-1}$ and standard deviation $1.5\pm0.1\,km\,s^{-1}$.

peak MALT-45 CS is outside of the data presented in Fujiyoshi et al. (2006); it is possible that the spatial resolution of our CS data is limiting our ability to interpret the physics of this region. However, it is interesting that the peak velocities of CS are quite different to H90 α; this may indicate complex structure of the source, and indeed this is discussed in Fujiyoshi et al. (2006).

The weak presence of NH_3 (1,1) emission is mysterious. The high CS/NH_3 ratio may be attributable to the region being at a higher temperature, preventing CS depletion. Lowe et al. (2014) attempted a NH_3 (1,1) and (2,2) analysis of this clump, but were unable to detect significant emission. They suggested that the relatively faint NH_3 emission could be due to extreme self-absorption. Lo et al. (2009) comment that in general, CS (2–1) and HCO^+ (1–0) have similar velocity structure, except at this location; the HCO^+ has a strong self-absorption feature. However, given that the source is clearly evolved, it is consistent with the other sources discussed in having little NH_3 emission.

4.1.4 Summary

The cause for the high ratios ($CS/NH_3 > 3$) in our analysis appears to stem from evolved regions of HMSF. The other clumps are more difficult to classify - Are they less evolved? Do they have significantly different temperatures or column densities? More analysis is needed, and will be presented in a future MALT-45 paper with CS clump analysis.

4.2 Comparing CS (1–0) with class I CH_3OH maser regions

Table 2 includes the integrated flux density of CS (1–0) in each maser region. The kinematic distance calculated for each source is used to determine the luminosities. Figure 12 compares the integrated CS intensity with the integrated class I CH_3OH maser intensity.

Figure 2 shows that most class I CH_3OH masers appear to be associated with a bright peak of CS emission (73/77

masers with $>0.11\,K$ of peak intensity CS). This is quantified (using integrated intensity) in Figure 12. However, there is no correlation observed between the relative intensity of a class I CH_3OH maser and its associated CS.

A class I CH_3OH maser with CS emission suggests association with a star-forming region, because sufficient gas and shocks exist to power their emission. However, without being able to associate these lines with other diagnostics of star formation, it is not certain that the masers are stimulated by star formation; cloud-cloud collisions have been found to stimulate class I CH_3OH emission (Sjouwerman, Pihlström & Fish 2010). While the possibility of being a non-star-forming maser extends to all candidates without additional tracers (such as class II CH_3OH masers), we expect that these are exceptional cases, and that the majority if not all class I CH_3OH masers in the MALT-45 sample are associated with star formation.

A comparison of class I and class II CH_3OH masers was undertaken by Voronkov et al. (2014), and found a broad Gaussian distribution of velocity differences. We have performed a similar analysis with the peak velocities of both CS and class I CH_3OH masers from the MALT-45 data. The resulting histogram of the velocity difference of CH_3OH with respect to CS is found in Figure 13. The distribution is approximated by a Gaussian with a mean velocity difference $0\pm0.2\,km\,s^{-1}$ and standard deviation $1.5\pm0.1\,km\,s^{-1}$. The median velocity difference is -0.1 $km\,s^{-1}$.

The FWHM of the population presented by Voronkov et al. (2014) is approximately $7.8\,km\,s^{-1}$, while ours is approximately $3.5\,km\,s^{-1}$. Because CS is a dense gas tracer, it will occur in cloud cores and thus trace systemic motions accurately. Given the resulting Gaussian of velocity differences, this means that class I CH_3OH masers are also good indicators of systemic velocities. Voronkov et al. (2010a) discuss class I CH_3OH masers having similar velocities to the quiescent gas, due to a small amount of gas actually being shocked in these regions. As is noted in Voronkov et al. (2014), Garay et al. (2002) indicate that CH_3OH emission arising without thermal SiO emission is due to mild

shocks, destroying dust grain mantles but not dust grain cores. Hence the dispersion in class I CH_3OH maser velocities is thought to be small, and is reflected here. This also indicates that the large dispersion seen by Voronkov et al. (2014) is likely due to the large class II CH_3OH maser velocity spread. This is readily explained by class II CH_3OH maser emission radiating from close to a high-mass young stellar object, and therefore having a higher dispersion.

The histogram in Figure 13 appears to have a slight blueshifted component. This is also discussed in Voronkov et al. (2014) as perhaps due to maser emission being easier to detect on the near-side of a cloud to the observer. While the median velocity offset is negative, it is statistically insignificant. A larger data set is required to determine if the blueshift phenomena is real or not.

4.3 Comparing class I CH_3OH maser regions with SiO (1–0)

As discussed in Section 1.1, SiO $v = 0$ is a good tracer of shocked gas and outflows. Regions of thermal SiO and positions of class I CH_3OH masers correlate weakly; 23 of 77 masers (30 per cent) have at least a 2σ peak of SiO emission. As class I masers are collisionally excited, it is perhaps not surprising to find some association with thermal SiO. However, the majority of masers are detected without SiO $v = 0$ emission. This could be due to: insufficient sensitivity to extended SiO emission; class I CH_3OH masers having stronger intensity than thermal SiO; or not all class I CH_3OH masers being associated with SiO $v = 0$ emission. Garay et al. (2002) found that thermal CH_3OH emission may be triggered by less energetic shocks, which destroy dust grain mantles but not their cores, which explains a lack of SiO emission. In more energetically shocked regions (such as a jet or molecular outflow), CH_3OH may not survive, which may explain SiO emission without CH_3OH.

Three regions with strong SiO emission (0.04 K) are not associated with any maser species: G331.02−0.42, G333.63−0.11 and G334.20−0.20. Each of these regions has a CS peak of at least 0.4 K ($> 10\sigma$), but no obvious infrared emission. Table 2 lists 28 class I CH_3OH masers with detected SiO emission, implying that these three regions without masers are in the minority. This could be due to the variability of any masers making them undetectable during observations, or that conditions in these regions are unfavourable for masers to exist.

It is clear that sensitivity to CH_3OH and/or SiO will play a part in the detectability of each. However, the fact that we see regions with both CH_3OH and SiO, regions with only CH_3OH masers and regions with only SiO emission suggests that there are multiple conditions under which each of these will exist. If we assume that all class I CH_3OH masers are associated with star formation, then given that the majority of masers are not associated with thermal SiO emission, these masers may be tracing weaker shocks that do not produce detectable SiO emission. 30 per cent of CH_3OH masers also show thermal SiO emission. It is not clear whether the masers and SiO are physically connected, although a reasonable interpretation is that the SiO originates in a jet, where as the masers are associated with the surrounding outflow. In a subsequent paper for MALT-45, maser follow-up observations will be conducted at high
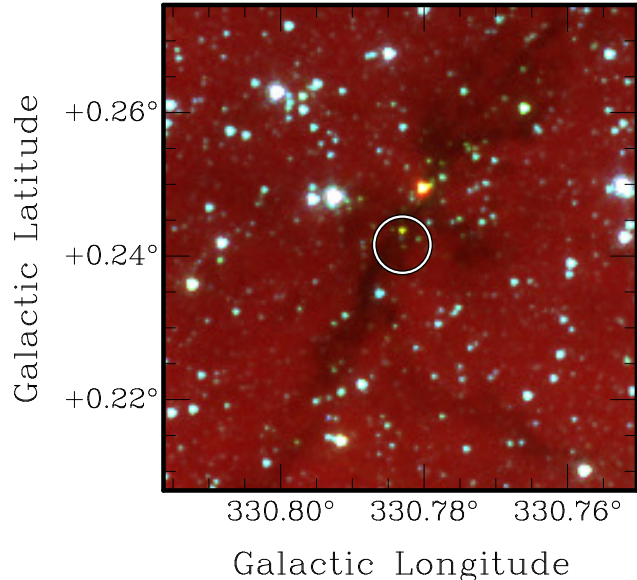

Figure 14. An example of a class I CH_3OH maser with associated "green" emission. This region is not classified as an EGO by Cyganowski et al. (2008), but may have similar properties. The circle represents 15 arcsec centred on the peak of the class I CH_3OH maser emission, which is the expected positional error.

spatial resolution. We will simultaneously observe SiO with greater sensitivity, and using this data we will more thoroughly investigate the association of class I CH_3OH masers and thermal SiO emission.

4.4 Class I CH_3OH maser comparison with GLIMPSE

GLIMPSE mapped the Galactic plane in four infrared bands (3.6, 4.5, 5.8 and 8.0 μm). These images are useful for investigating potential relationships between infrared emission and MALT-45 detections. A common example of how GLIMPSE data is used in star formation research is by combining the 3.6, 4.5 and 8.0 μm bands in a three-colour image (blue, green and red, respectively) to reveal EGOs (extended green objects). As discussed in Cyganowski et al. (2008), EGOs have a strong correlation with class I CH_3OH maser regions.

The catalogue provided by Cyganowski et al. (2008) was used to investigate the presence of EGOs over the survey region. The catalogue covers $10° \leqslant l \leqslant 65°$ and $295° \leqslant l \leqslant 350°$, $b = \pm1.0°$, and lists 22 candidate EGOs within the MALT-45 survey region. Of the 77 class I masers found by MALT-45, 12 are associated with an EGO. Association is credited for any spatial overlap within 60 arcsec. Of the 12 EGO-associated class I CH_3OH masers, 11 were previously known (G330.95−0.18 is new). EGOs are classified by visual inspection and as such are intrinsically subjective. However, it is clear that many of the new class I CH_3OH maser detections are associated with GLIMPSE sources with "green" (i.e. 4.5 μm excess) emission; see Figure 14 for an example source. Cyganowski et al. (2009) explains that the green emission band of GLIMPSE contains both H_2 and CO (1–0) lines, which are excited by shocks. Indeed, some of the new masers detected by MALT-45 have similar "green" emission as with EGOs, although less prominently
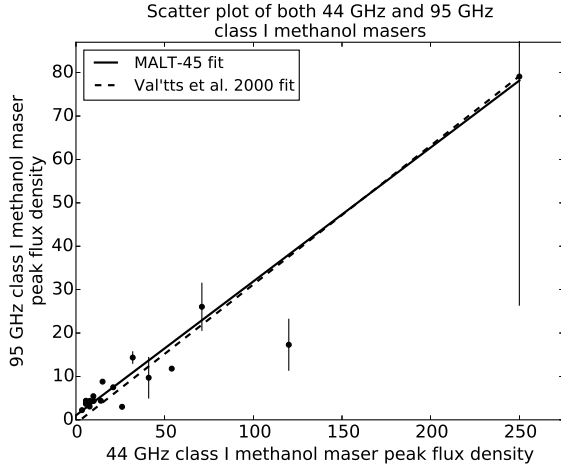
Figure 15. A scatter plot of 44 GHz class I CH_3OH masers from MALT-45 with known 95 GHz class I CH_3OH maser emission. There are 19 masers with both 44 and 95 GHz emission. The line of best fit for these data is plotted alongside the line of best fit presented by Val'tts et al. (2000). Vertical lines indicate the minimum and maximum recorded values for 95 GHz masers, if available, on top of the plotted average. Units of peak flux density are in Jy.

Figure 16. The luminosities of associated class I and class II methanol masers plotted against each other. No significant correlation is observed. Units of luminosity for the masers are $Jy\,kpc^{-2}$, using peak flux densities.

so. This shows a close association between shocks traced by EGOs and class I CH_3OH masers.

4.5 95 GHz class I CH_3OH masers

Val'tts et al. (2000) found a relationship between the peak flux density of the 95 and 44 GHz class I methanol masers (which come from the same transition family). They found that the peak flux density of 44 GHz masers is approximately three times greater than the 95 GHz masers.

Information for 95 GHz class I CH_3OH masers towards MALT-45 44 GHz masers are obtained from Val'tts et al. (2000); Ellingsen (2005) and Chen et al. (2011). In total, we have 19 class I maser sources with both 44 and 95 GHz peak flux densities. When faced with more than one peak flux density over various epochs, we use the average of all values. Analysing the distribution in Figure 15, we find that our results agree with those of Val'tts et al. (2000). Our line of best fit is $P_{95} = 0.31 \times P_{44} + 1.0$, with an r^2-value of 0.98, while the Val'tts et al. (2000) fit is $P_{95} = 0.32 \times P_{44} - 8.1$, with an r^2-value of 0.53. The uncertainty of our fitted slope is ±0.01. Note that our fit does not use the 44 GHz maser with 120 Jy; if we do include it, our fit becomes $P_{95} = 0.28 \times P_{44} + 1.0$, with an r^2-value of 0.91 and uncertainty ±0.02. This is not significantly different, but our slope closely agrees with Val'tts et al. (2000) when the outlier is omitted.

4.6 Class I CH_3OH maser associations

In this section, we discuss other maser species and transitions and their association with the class I CH_3OH masers detected in MALT-45. Association with each maser is credited if the emission in question is within 60 arcsec of the class I maser position.
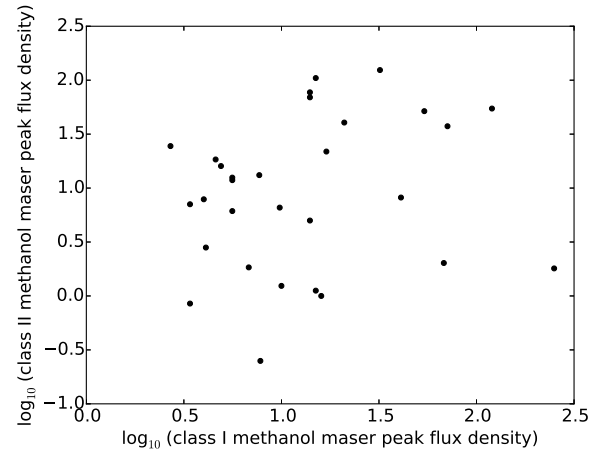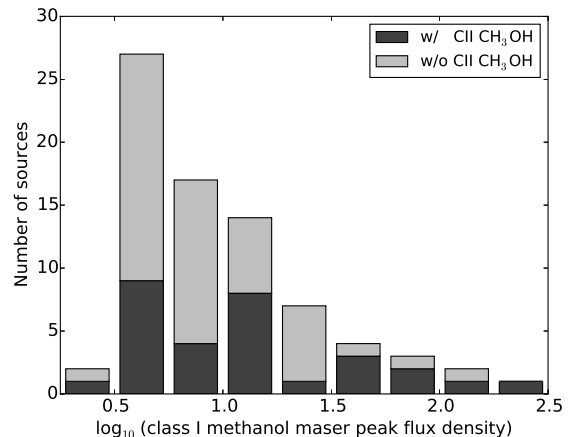

Figure 17. A stacked histogram of class I methanol masers with and without class II methanol masers. This plot shows that class II masers can be associated with a wide range of class I intensities.

4.6.1 Class II masers from the MMB

In the past, class I methanol masers have been identified from targeted searches towards class II maser sites (Ellingsen 2005). For the first time, we are able to make an unbiased comparison of the rate at which each class of methanol maser occurs and their degree of overlap.

Within the MALT-45 survey region, 54 6.7 GHz class II methanol masers have been detected by the MMB (Caswell et al. 2011). To compare against MALT-45 class I maser regions, 7 class II masers have been grouped together into "clusters", as they are close together (within 60 arcsec). The clusters containing grouped masers are G330.88−0.37, G331.54−0.07, G332.30−0.09, G333.13−0.44 and G333.23−0.06. While the velocities of each maser site grouped together may be different, there is significant overlap in the range of emission (not greater than $9\,km\,s^{-1}$ apart). Without high-resolution positions, inferring which class II maser is associated with the class I emission is

difficult, and it is more practical to only compare their clustered position, especially as a class I CH$_3$OH maser is almost certainly associated with the class II source. Therefore, we compare 47 class II methanol masers positions against the 77 class I sources detected in MALT-45. There are 28 class I CH$_3$OH masers associated with the clusters, and 16 of these class I masers are new; see Table 2. An association exception is made for G331.13−0.25, where the class II CH$_3$OH maser is slightly further offset than 60 arcsec from the MALT-45 class I CH$_3$OH maser position, but is well studied and known to be related (Ellingsen 2005; Voronkov et al. 2014). Additionally, the next closest class I and class II CH$_3$OH maser pair is approximately 100 arcsec, which aids to rule out misassociation. Thus, 60 per cent of class II masers have a class I counterpart (28/47), while approximately 36 per cent of class I masers have a class II counterpart (28/77).

Ellingsen (2005) reports a 38 per cent association of class II sources with a 95 GHz class I maser counterpart. Given that the 44 GHz species is typically stronger than the 95 GHz transition, and that the MALT-45 sensitivity is better, we perhaps expect our reported class II-to-class I association to be greater. As discussed in Section 4.5, Val'tts et al. (2000) finds the relative peak flux density of 95 GHz class I CH$_3$OH masers to 44 GHz class I CH$_3$OH masers to be approximately one-third. Assuming Ellingsen (2005) had a sensitivity cutoff for 95 GHz masers at 3 Jy, we can limit the results of the 44 GHz population by a 9 Jy cutoff. There are 17 44 GHz masers with a peak flux density greater than 9 Jy associated with a class II CH$_3$OH maser (36 per cent), which is only slightly lower than the proportion of associations found by Ellingsen (2005). Therefore, our results are reasonably consistent. Considering that the MALT-45 sensitivity to class I CH$_3$OH masers is better than that of Ellingsen (2005) by approximately a factor of 2, and that we search for 44 GHz masers instead of 95 GHz masers, we are assured that there is a higher association rate than previously reported.

The luminosities of class I and class II CH$_3$OH masers were compared, but no correlation was found (r^2-value of 0.03); see Figure 16. The relative populations for class I masers with and without a class II source are compared in Figure 17; the histogram reveals that class II sources are associated with a wide range of class I brightnesses, which reaffirms the lack of correlation. With sensitive, targeted 44 GHz observations of class II masers, more data can be collected for a better analysis. Note that the search radius should be at least an arcmin to cover the range of separations between class I and class II masers; see Section 4.2 of Voronkov et al. (2014).

4.6.2 H$_2$O masers from HOPS

Water masers are another maser species that are collisionally excited. Therefore, we might expect a close association between class I methanol and water masers. HOPS has found H$_2$O masers in an untargeted way, and catalogues their findings into three association groups: star-forming, evolved star, and "unknown" (Walsh et al. 2014). Breen et al. (2010) also presents a catalogue of H$_2$O masers, typically associated with class II CH$_3$OH masers and/or OH masers.

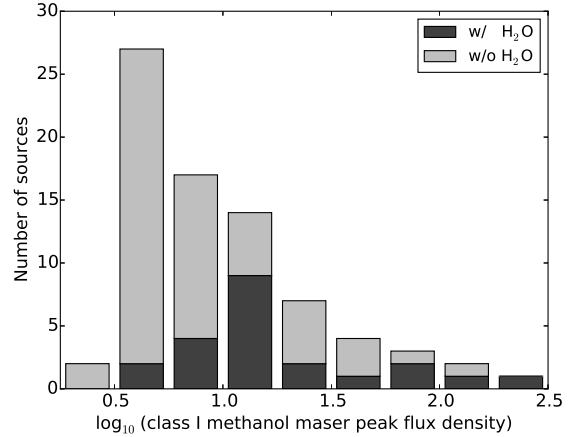HOPS has detected a total of 48 H$_2$O masers within the MALT-45 survey region (Walsh et al. 2011, 2014). Of these,

Figure 18. A stacked histogram of class I methanol masers with and without H$_2$O masers. This plot shows that H$_2$O masers tend to be associated with brighter class I methanol masers.

HOPS has classified 10 as being associated with an evolved star, leaving 38 as star-forming or "unknown". Including the Breen et al. (2010) detections brings the total to 71, but there is a large overlap with the HOPS catalogue, as well as many H$_2$O masers near to others (within 60 arcsec). Similar to the MMB class II CH$_3$OH masers, after grouping masers into clusters, we compare MALT-45 class I CH$_3$OH masers against a total of 43 H$_2$O maser clusters.

Of these 43 H$_2$O maser clusters, 27 are associated with a class I CH$_3$OH maser (63 per cent). It is possible that the class I CH$_3$OH population have more H$_2$O maser associations, but have not been found yet. Breen et al. (2010) targeted observations towards known sources, and HOPS has a lower-bound sensitivity between 5 and 10 Jy. Follow-up observations for H$_2$O masers towards new class I CH$_3$OH masers may be productive in identifying new H$_2$O masers.

In the HOPS catalogue recently published (Walsh et al. 2014), the water masers G331.86+0.06 and G333.46−0.16 were not redetected in the high-resolution follow-up survey. The G333.46−0.16 water maser is associated with a MALT-45 class I CH$_3$OH maser, but this was a known class I CH$_3$OH maser region (along with other maser species). The G331.86+0.06 water maser, however, is slightly offset from a new class I CH$_3$OH maser. The offset is enough to not be included as an association, but it lends credence that this variable water maser is likely highlighting star-forming activity.

4.6.3 OH masers from Sevenster et al. (1997) and Caswell et al. (1998)

Voronkov et al. (2010a) discuss the positioning of class I methanol maser emission on a HMSF evolutionary timeline, especially compared to other masers. Class II methanol masers have been characterised well in terms of their position in a HMSF timeline, associated with millimetre sources, but typically not H II regions. Unlike class II masers, class I masers are currently thought to be associated with both early- and late-type HMSF. This stems from finding class I masers associated with outflows, but also with OH masers.
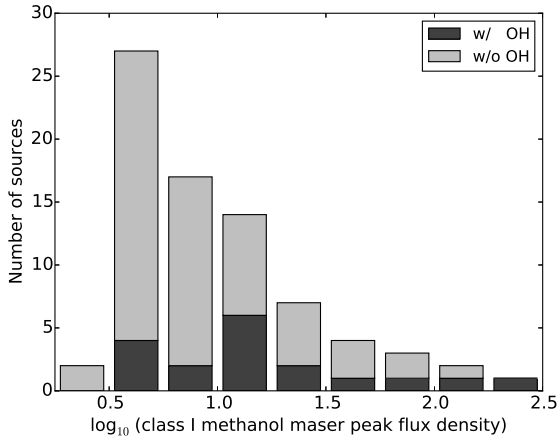
Figure 19. A stacked histogram of class I methanol masers with and without OH (1612, 1665, or 1667 MHz) masers. OH masers appear to be associated with a wide range of class I methanol masers.

Figure 20. Venn diagram of all discussed maser region associations. The majority of maser regions have a class I CH_3OH component, particularly with class II CH_3OH as well, but there is a large population of class I masers without any associations.

4.6.4 Summary of star-formation maser associations

A Venn diagram of the maser associations can be seen in Figure 20. There appears to be a strong overlap between class I and class II CH_3OH masers, with and without the presence of H_2O and/or OH masers. This may suggest that the majority of class II CH_3OH masers are associated with class I CH_3OH masers because of an abundance of CH_3OH. The smaller population of class II CH_3OH masers without class I CH_3OH emission (40 per cent; 19/47) may indeed have no association, or even weaker class I CH_3OH emission than is detected by MALT-45.

There is a large population of class I CH_3OH masers without any other maser counterpart. As discussed, these may highlight non-star-forming phenomena, young regions of HMSF, or low mass star-forming regions. However, given the strong association with CS seen in Figure 3 and with other HMSF masers seen in Figure 20, the majority of class I CH_3OH masers are likely associated with HMSF.

Figures 17, 18 and 19 show the luminosity population of class I CH_3OH masers as stacked histograms. Generally, the presence or absence of other maser transitions does not appear to correlate with the class I CH_3OH maser luminosity.

Titmarsh et al. (2014) discuss the placement of H_2O masers within an evolutionary timeline for HMSF, and concluded that they are not likely to be associated with any specific phase of a timeline, but rather dependant on the environment. As H_2O masers are collisionally excited like class I CH_3OH masers, and class I masers are associated with a wide range of other species (with and without class II CH_3OH, OH), we tend to agree that the environment plays perhaps the predominant role in determining the likelihood of a region having an associated class I CH_3OH maser rather than the evolutionary phase.

Investigation of the peak flux densities and luminosities of class I CH_3OH masers versus class II CH_3OH, H_2O and OH masers does not reveal any relation. Investigation will be performed again in a subsequent MALT-45 maser follow-up paper, where maser regions can be better associated and flux density calibration is able to be more accurately determined.

To date, no unbiased comparison between OH and class I methanol masers has been performed. With the first unbiased sample of class I masers, we are able to analyse the relative populations and perhaps refine class I masers on an evolutionary timeline. Voronkov et al. (2010a) mentions that class I masers associated with OH masers are known primarily due to the class II methanol maser emission present, as most class I sources have been found toward class II sources. Caswell et al. (1997) discuss how OH favoured maser regions have a greater number of associated H II regions than class II masers, indicating that OH masers typically signpost later stages of an evolutionary timeline than class II masers. Combining the OH masers found by Sevenster et al. (1997) and Caswell et al. (1998), there are 16 star-forming OH masers within the MALT-45 survey region. The other OH masers in Sevenster et al. (1997) and Caswell et al. (1998) are associated with evolved OH/IR stars, determined from SIM-BAD and individual source descriptions within Caswell et al. (1998). 94 per cent (15/16) of star-forming OH masers are associated with a class I CH_3OH maser. Of these 15, only 2 masers are without a 6.7 GHz class II methanol maser (13 per cent; G331.50−0.10 and G333.59−0.21). It is difficult to contrast maser regions containing OH but not class II methanol, as almost every OH maser in the survey region is associated with a class II CH_3OH maser. If a population of OH masers without class II CH_3OH was isolated, a better comparison with class I CH_3OH could be established. The MALT-45 survey results merely indicate that class I CH_3OH is associated with all maser species found.

There are 30 class I CH_3OH maser regions with associated class II CH_3OH or OH maser emission, indicating late stages of star formation. The remaining 47 masers are unaccounted for; if these are all associated with early-type star-formation, then class I CH_3OH masers appear to be more closely associated with earlier stages in an evolutionary timeline.
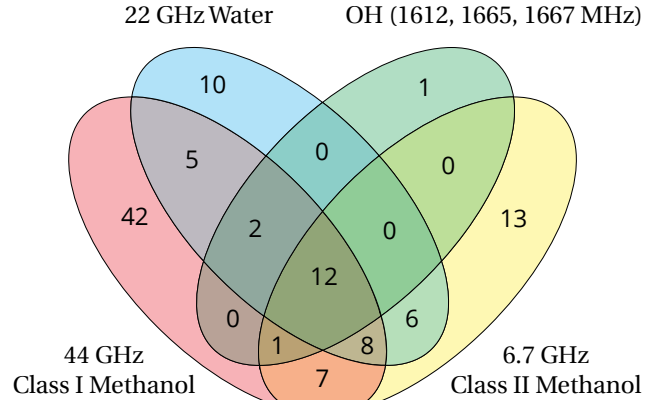
4.7 SiO $v = 1, 2, 3$ maser associations

MALT-45 has detected 47 regions with at least one of the vibrationally excited lines $v = 1, 2, 3$ of SiO (1–0) maser emission. Of these, 4 are associated with a OH maser (all 1612 MHz, G331.60−0.14 has an additional 1665 MHz), and 8 are associated with a H_2O maser. OH and H_2O masers are common companions with evolved infrared stars (Caswell et al. 1998; Walsh et al. 2014), and indeed GLIMPSE reveals that all SiO maser regions have an infrared star associated within 30 arcsec of the peak maser position. There is no overlap of SiO masers associated with both an OH and H_2O maser. The population presented in this paper associated with OH and H_2O masers is insufficient to perform correlation tests upon. None of the SiO masers detected have been reported previously; thus, MALT-45 is a productive survey for identifying evolved stars not found in other searches.

The SiO $v = 1$ line generally appears to be the strongest of the three maser lines, and is the most common detection. There are eleven cases where the $v = 2$ line is stronger than $v = 1$, and two regions contain only $v = 2$ emission. This result is somewhat unexpected, as generally the lower v transitions should be brighter than the higher v transitions. Gray et al. (2009) predict that SiO masers should have brightness decreasing with $v = 1, 2, 3$, and the $v = 2$ is often weaker due to overlap with a water line. Neither of the two regions with only SiO $v = 2$ emission have other masers associated, but the sub-population of SiO regions with brighter $v = 2$ than $v = 1$ have three H_2O masers and two OH masers associated. This is almost half of all masers associated with SiO regions. However, we currently cannot explain why some $v = 2$ masers are stronger than their $v = 1$ counterparts. Only three $v = 3$ lines are detected, and these are all quite weak, especially compared to the $v = 1, 2$ lines within the same region; it appears that this line is difficult to detect without sensitive observations.

The only SiO maser with nearby CH_3OH masers is G333.90−0.09, but is separated by 33 arcsec. The same SiO maser is 13 arcsec from a Sevenster 1612 MHz OH maser, which is cospatial with a star in GLIMPSE. As the nearby class I and class II CH_3OH masers are only 4 arcsec apart but separated from the star, we consider both pairs of masers to not be associated.

5 SUMMARY AND CONCLUSIONS

MALT-45 has successfully probed the Galactic plane for CS (1–0), 44 GHz class I methanol masers, and the SiO (1–0) family of $v = 0, 1, 2, 3$ lines. This is the first survey to produce a large scale unbiased map of CS, and is the first untargeted search of class I CH_3OH masers and SiO emission. Further publications will reveal the full 7 mm star-forming environment, through the remaining lines mapped by this survey. With time, MALT-45 could be extended to map more of the Galactic plane, revealing more about the nature of star formation within our Galaxy. With the current survey, we have determined:

(i) Across the survey region, the CS/NH_3 ratio is low in the centres of many clumps, but higher at the edges. This is likely due to a combination of increased NH_3 abundance and CS being depleted and/or becoming optically thick in the centres of clumps;

(ii) A large population of class I methanol masers are not associated with other masers (55%);

(iii) Class I methanol masers are good indicators of systemic velocities;

(iv) Class I methanol masers are found towards most known class II methanol, water and hydroxyl masers within the survey region. Thus, positioning class I methanol on a maser timeline of HMSF is difficult, and the occurrence of class I methanol masers is perhaps more likely due to environmental factors;

(v) Silicon monoxide masers associated with evolved stars are most commonly detected in their $v = 1$ vibrational mode. When a region contains more than one vibrational mode, the intensity typically descends with vibrational mode ($v = 1, 2, 3$). However, we find two cases where we only detect $v = 2$ and eleven cases where both $v = 1$ and $v = 2$ are detected, but the $v = 2$ is stronger.

REFERENCES

Bergin, E. A., Ciardi, D. R., Lada, C. J., Alves, J., 2001, ApJ, 557, 209-225

Bronfman, L., Nyman, L.-A., May, J., 1996, A&APS, 115, 81

Breen, S. L., Caswell, J. L., Ellingsen, S. P., Phillips, C. J., 2010, MNRAS, 406, 1487-1532

Breen, S. L. et al., 2013, MNRAS, 435, 524-530

Burton, M. G. et al., 2013, Publications of the Astronomical Society of Australia, 30, 44

Caswell, J. L., 1997, MNRAS, 289, 203-224

Caswell, J. L., 1998, MNRAS, 297, 215-235

Caswell, J. L. et al., 2011, MNRAS, 417, 1964-1995

Chen, X., Ellingsen, S. P., Shen, Z. Q., Titmarsh, A., Gan, C. G., ApJS, 196, 9

Chin, Y. N., Henkel, C., Whiteoak, J. B., Langer, N. Churchwell, E. B., 1996, A&A, 305, 960

Cooper, H. D. B. et al., 2013, MNRAS, 430, 1125-1157

Csengeri, T. et al., 2014, A&A, 565, A75

Cyganowski, C. J. et al., 2008, AJ, 136, 2391

Cyganowski, C. J., Brogan, C. L., Hunter, T. R., Churchwell, E., 2009, ApJ, 702, 1615-1647

Dame, T. M., Hartmann, D., Thaddeus, P., 2001, ApJ, 547, 792-813

Dawson, J. R. et al., 2014, MNRAS, 439, 1596-1614

Ellingsen, S., 2005, MNRAS, 359, 1498-1516

Ellingsen, S., 2006, ApJ, 638, 241-261

Elitzur, M., 1992, ARA&A, 30, 75-112

Evans, II, N. J., 1999, ARA&A, 37, 311

Fujiyoshi, T. et al., 2006, MNRAS, 368, 1843-1855

Fuller, G., Myers, P., 1993, ApJ, 418, 273

Gan, C., Chen, X., Shen, Z., Xu, Y., Ju, B., 2013, ApJ, 763, 2

Garay, G., Mardones, D., Rodríguez, L. F., Caselli, P., Bourke, T. L., 2002, ApJ, 567, 980-998

Garay, G., Mardones, D., Bronfman, L., May, J., Chavarría, L., Nyman, L.-Å., 2010, ApJ, 710, 567-582

Gray, M. D. et al., 2009, MNRAS, 394, 51-66

Green, J. A. et al., 2009, MNRAS, 392, 783

Green, J. A., McClure-Griffiths, N. M., 2011, MNRAS, 417, 2500-2553

Green, J. A. et al., 2012, MNRAS, 420, 3108-3125

Ilee, J. D. et al., 2013, MNRAS, 429, 2960-2973

Jackson, J. M. et al., 2006, ApJS, 163, 145

Jordan, C. H. et al, 2013, MNRAS, 429, 469-481

Kalenskii, S. V. et al., 2010, MNRAS, 620, 613-620

Kauffmann, J., Pillai, T., 2010, ApJL, 723, L7-L12

Kurtz, S., Hofner, P., Alvarez, C. V., 2004, ApJS, 155, 149-165

Lada, C., Lada, E., 2003, ARA&A, 41, 57-115

Lilley, A. E., Palmer, P., 1968, ApJS, 16, 143

Lo, N. et al., 2009, MNRAS, 395, 1021

Lowe, V. et al., 2014, MNRAS, 441, 256-273

Lumsden, S. L. et al., 2013, ApJS, 208, 11

Martin-Pintado, J., Bachiller, R., Fuente, A., 1992, A&A, 254, 315

Matthews, L. D. et al., 2007, in Chapman J. M., Baan W. A., eds, IAU Symp. 242, Astrophysical Masers and their Environments. Cambridge Univ. Press, Cambridge, p. 130

McClure-Griffiths, N. M. et al., 2005, ApJS, 158, 178-187

Messineo, M., Habing, H. J., Sjouwerman, L. O., Omont, A., Menten, K. M., 2002, A&A, 393, 115-128

Minier, V., Ellingsen, S. P., Norris, R. P., Booth, R. S., 2003, A&A, 403, 1095-1100

Müller, H. S. P., Schlöder, F., Stutzki, J., Winnewisser, G. 2005, Journal of Molecular Structure, 742, 215

Peretto, N., Fuller, G. A., 2009, A&A, 505, 405-415

Pihlström, Y. M., Sjouwerman, L. O., Frail, D. A., Claussen, M. J., Mesler, R. A., McEwen, B. C., 2014, ApJ, 147, 73

Purcell, C. R. et al., 2012, MNRAS, 426, 1972-1991

Purcell, C. R. et al., 2013, ApJS, 205

Reid, M. J. et al., 2009, ApJ, 700, 137-148

Rodgers, A. W., Campbell, C. T., Whiteoak, J. B., MNRAS, 1960, 121, 103

Sevenster, M. N., Chapman, J. M., Habing, H. J., Killeen, N. E. B., Lindqvist, M., A&AS, 1997, 124, 509-515

Sjouwerman, L. O., Pihlström, Y. M., Fish, V. L., 2010, ApJL, 710, L111-L114

Slysh, V. I., Kalenskii, S. V., Valtts, I. E., Otrupcek, R., 1994, MNRAS, 268, 464

Tafalla, M., Myers, P. C., Caselli, P., Walmsley, C. M., Comito, C., 2002, ApJ, 569, 815

Tafalla, M., Myers, P. C., Caselli, P., Walmsley, C. M., 2004, A&A, 416, 191-212

Taylor, S. D., Morata, O., Williams, D. A., 1998, A&A, 336, 309-314

Titmarsh, A. M., Ellingsen, S. P., Breen, S. L., Caswell, J. L., Voronkov, M. A., 2014, MNRAS, 443, 2923-2939

Urquhart, J. S. et al., 2010, Publications of the Astronomical Society of Australia, 27, 321-330

Val'tts, I. E., Ellingsen, S. P., Slysh, V. I., Kalenskii, S. V., Otrupcek, R., Larionov, G. M., 2000, MNRAS, 317, 315-332

Voronkov, M. A., Caswell, J. L., Ellingsen, S. P., Sobolev, A. M., 2010, MNRAS, 405, 2471-2484

Voronkov, M. A., Caswell, J. L., Britton, T. R., Green, J. A., Sobolev, A. M., Ellingsen, S. P., 2010, MNRAS, 408, 133-138

Voronkov, M. A., Caswell, J. L., Ellingsen, S. P., Green, J. A., Breen, S. L., 2014, MNRAS, 439, 2584-2617

Walsh, A. J., Burton, M. G., Hyland, A. R., Robinson, G., 1998, MNRAS, 301, 640

Walsh, A. J. et al., 2011, MNRAS, 416, 1764

Walsh, A. J. et al., 2014, MNRAS, 442, 2240

Wilson, W. E. et al., 2011, MNRAS, 416, 832

Zapata, L. A., Menten, K., Reid, M., Beuther, H., 2009, ApJ, 691, 332

Zinnecker, H., Yorke, H. W., 2007, ARA&A, 45, 481